

1 **Occurrence frequency of subcritical Richardson number**
2 **assessed by global high-resolution radiosonde and ERA5**
3 **reanalysis**

4
5 Jia Shao¹; Jian Zhang^{2*}; Wuke Wang³; Shaodong Zhang⁴; Tao Yu²; Wenjun Dong^{5,6}

6
7
8 ¹ College of Informatics, Huazhong Agricultural University, Wuhan 430070, China

9 ² Hubei Subsurface Multi-scale Imaging Key Laboratory, School of Geophysics and
10 Geomatics, China University of Geosciences, Wuhan 430074, China

11 ³ School of environmental studies, China University of Geosciences, Wuhan 430074,
12 China

13 ⁴ School of Electronic Information, Wuhan University, Wuhan 430072, China

14 ⁵ Center for Space and Atmospheric Research (CSAR), Embry-Riddle Aeronautical
15 University, Daytona Beach, FL, USA

16 ⁶ Global Atmospheric Technologies and Sciences (GATS), Boulder, CO, USA

17
18
19
20 Correspondence to:

21 Dr. Jian Zhang (Email: zhangjian@cug.edu.cn)

29 **Abstract.** Kelvin Helmholtz instability (KHI) is most likely to be the primary source
30 for clear-air turbulence that is of importance in pollution transfer and diffusion and
31 aircraft safety. It is indicated by the critical value of the dimensionless Richardson (Ri)
32 number, which is predicted to be 1/4 from linear stability analysis. However, Ri is fairly
33 sensitive to the vertical resolution of the dataset; a higher resolution systematically
34 leads to a finer structure. The study aims to evaluate the performance of ERA5
35 reanalysis in determining the spatial-temporal variabilities of subcritical Ri by
36 comparing it against a near-global high-resolution radiosonde dataset during years 2017
37 to 2022 and further highlight the global climatology and dynamical environment of
38 subcritical Ri . Overall, the occurrence frequency of $Ri < 1/4$ is inevitably underestimated
39 by the ERA5 reanalysis over all climate zones at all heights from near-ground
40 atmosphere up to 30 km, compared to radiosonde, due largely directly to the severe
41 underestimation in wind shears. Otherwise, the occurrence frequency of $Ri < 1$ in ERA5
42 is climatologically consistent with that from $Ri < 1/4$ in radiosondes in the free
43 troposphere, especially over the midlatitude and subtropics in the Northern/Southern
44 Hemisphere. Therefore, we argue that threshold value of Ri could be approximated as
45 1 rather than 1/4 when using ERA5-based Ri as a proxy for KHI. The occurrence
46 frequency of subcritical Ri revealed by both datasets exhibits significant seasonal cycles
47 over all climate zones. In addition, it is positively correlated with the standard
48 derivation of orography at low-levels and is exceptionally strong over the Niño 3 region
49 at heights of 6–13 km. Furthermore, a high occurrence of subcritical Ri would likely be
50 accompanied by strong wind speeds and intensive orographic or non-orographic gravity
51 waves.

52
53 **Key words:** High-resolution radiosonde; ERA5 reanalysis; Wind shears; Richardson
54 number; Gravity waves

55
56
57

58 Introduction

59 Kelvin Helmholtz instability (KHI) is a common phenomenon in the atmospheric
60 boundary layer and the free atmosphere (Muschinski and Wode, 1998), and its
61 wavelengths and depths span a wide range of scales throughout the atmosphere, varying
62 from few meters or less to ~~tens+0s~~ of km (Fritts et al., 2011). It contributes to vertical
63 mixing of heat, momentum, and constituents, and it acts to limit the maximum shears,
64 just to name a few (Fritts et al., 2011). KHI along with gravity wave (GW) breaking are
65 the most recognized instabilities in stably stratified flows (Fritts and Rastogi, 1985).
66 KHI arises preferentially from micro- and mesoscale wind shear intensification, with
67 ~~the~~ maximal occurrence frequency near synoptic scale upper-level frontal zones near
68 jet streams, with mountain waves, and above the tops of severe thunderstorms (North
69 et al., 2014). Large wind shears ~~areis~~ commonly associated with regions where stability
70 changes rapidly (e.g., near the top of the boundary layer) and the large wind gradient in
71 jet streams (Grasmick and Geerts, 2020). In a changing climate, wind shears ~~s~~ in the
72 North Atlantic upper-level jet stream could be increased (Lee et al., 2019), which may
73 increase clear-air turbulence at cruise altitudes. In turn, KHI can reduce wind shears
74 and alter tracer gradients where turbulence and mixing are most intense (Fritts et al.,
75 2022).

76 KHI influences depend on the spatial scales at which they lead to turbulence (Fritts
77 et al., 2022). Turbulence is by far the most common cause of serious injuries to aircraft
78 (Williams and Joshi, 2013). Convective instability, shear instability, KHI, and GW
79 breaking are known to be the major sources for turbulence (Sharman et al., 2012; Ko et
80 al., 2019; 2022; Lazarus et al., 2021). KHI requires a sufficiently large Reynolds
81 number and a Richardson (Ri) number sufficiently below $1/4$ to enable KHI formation
82 and subsequent secondary instability leading to turbulence (Fritts et al., 2022). Ri is not
83 a good guide to instability character in general, and $Ri > 1/4$ does not assure flow stability
84 for superpositions of mean and GW motions. Despite these caveats, $Ri < 1/4$ does
85 provide a reasonable guide to expected local KHI structure in cases where clear KH

86 billows arise, according to the simulation in the mesosphere and lower thermosphere
87 region (Fritts et al., 2014). Values of Ri close to zero favor strong instability, deep
88 billows, and relatively intense turbulence, whereas values of Ri closer to 1/4 favor weak
89 instability, shallow billows (Fritts et al., 2011). The Richardson number criterion can
90 be applied as a turbulence diagnostic in numerical model outputs (e.g., Sharman and
91 Pearson, 2017), and it has been used as such in climatological studies on the occurrence
92 of clear air turbulence (Jaeger and Sprenger, 2007). Kunkel et al. (2019) includes a brief
93 discussion on the capability of ECMWF models based on case studies to resolve
94 subcritical Richardson numbers, and argues that the threshold value of Ri (Rit) taken as
95 1 might be a good proxy for observed KHI. A very recent study by Lee et al. (2023)
96 also sets Rit from 0–1 in their climatology on the upper troposphere and lower
97 stratosphere turbulence diagnostics. Moreover, Zhang et al. (2022) shows that over half
98 of turbulence exists below $Ri < 1$ when the environment is beneficial for the development
99 of turbulence.

100 Turbulent mixing is of crucial importance to mass, energy, momentum transfer, the
101 dispersion of pollutants, and stratosphere-troposphere exchange. In numerical models,
102 turbulent dissipation rate, turbulent diffusivity and other parameters representing
103 turbulent mixing efficiency are the most basic parameters, which need to be accurately
104 parameterized to evaluate the impact of turbulence effect on matter and energy
105 distribution (Gavrilov et al., 2005). However, due to the intermittent nature of
106 turbulence it is generally not resolved in (global) numerical weather prediction models,
107 even at nowadays common/states of the art horizontal resolutions of the order of tens
108 of kilometers (Sandu et al., 2019), and it presents a challenge both in observation and
109 numerical modeling (Sharman et al., 2012; Homeyer et al., 2014; Plougonven and
110 Zhang, 2014). For this reason, the indices of turbulence, such as large wind shears,
111 small Ri and the negative squared Brunt-väisälä frequency, could be a great tool to
112 characterize turbulence (Jaeger et al., 2007).

113 The Richardson number is estimated by the finite differences across thin layers and
114 is quite sensitive to the vertical resolution of measurements (Haack et al., 2014). Thus,
115 a proper estimation of Ri requires a high-resolution measurement of temperature and

116 wind speed. The near-global distributed radiosonde site offers a unique opportunity to
117 investigate the climatology of subcritical Ri occurrence frequency. The overview of
118 subcritical Ri occurrence by using a near-global high-resolution (10-m) radiosonde data
119 was presented in Zhang et al. (2022), and a close association between subcritical Ri
120 occurrence frequency and turbulence fraction has been found. However, the global
121 climatology characteristic of subcritical Ri remains most unclear, especially over
122 oceans where the radiosonde network has a poor coverage.

123 By comparison, ERA5 global reanalysis can provide a seamless coverage of
124 temperature and wind, and it is the latest generation of the European Centre for
125 Medium-Range Weather Forecasts (ECMWF) atmospheric reanalysis and is based on
126 the state-of-the-art Integrated Forecasting System (IFS) Cy41r2 (Hersbach et al., 2020;
127 Gu et al., 2023). Its predecessor, ERA-Interim, was found in particular wind shear a
128 factor of 2–3 lower simulated based on high-resolution radiosondes (Houchi et al.,
129 2010). Moreover, results show that whatever the location and the geophysical
130 conditions considered, biases between ERA-Interim and balloon wind measurements
131 increase as a function of altitude (Duruiseau et al., 2017). Recent studies have
132 suggested that the structure and variability of the trade winds in the lower troposphere
133 are reasonably reproduced in the ERA5 reanalysis based on the EUREC4A field
134 campaign (Savazzi et al., 2022). However, the similar comparison between ERA5 and
135 high-resolution radiosonde across a near-global area has largely been undetermined.
136 The proper estimation of wind shear and Brunt-Väisälä frequency is essential for the
137 determination of Ri .

138 Thus, our objectives are to: (1) Evaluate the performance of ERA5 at different
139 heights and climate zones in estimating wind shear and small Richardson number
140 occurrence frequencies, in comparison with a large high-resolution radiosonde dataset
141 spanning the years from 2017 to 2022. (2) Based on the validation and comparison
142 results, we pose a question: how to use ERA5 for subcritical Ri estimation? (3) The
143 global climatology of subcritical Ri occurrence based on versatile measurements and
144 model products. (4) The dynamic environment (GWs and mean flow) of subcritical Ri .
145 ~~These works would be valuable for the understanding of the global distribution of~~

~~subcritical Ri , and furthermore, turbulence fraction.~~ To this end, this analysis is organized as follows. Section 2 shows the data and methods used. Section 3 represents the climatological variation of subcritical Ri and its comparison with radiosonde. Section 4 ends with a summary.

2 Data and methods

2.1 High-resolution radiosonde dataset

As described in Guo et al. (2021) and Zhang et al. (2022), a high vertical resolution radiosonde (HVRRS) dataset gained from several organizations was adopted, spanning January 2017 to October 2022, in a total of 5.8 years. The organizations include the China Meteorological Administration (CMA), the U.S. National Oceanic and Atmospheric Administration (NOAA), the Global Climate Observing System (GCOS) Reference Upper-Air Network (GRUAN), the Centre for Environmental Data Analysis of the United Kingdom (CEDA), University of Wyoming, Deutscher Wetterdienst, and ECMWF. In total, around 0.95 million radiosonde profiles from 434 radiosonde stations released at regular synoptic times of 0000 UTC and 1200 UTC were collected to determine the value of Ri . These profiles were sampled at 0.5 Hz or 1 Hz, corresponding to a vertical resolution of approximately 10 m or 5 m. Thus, all the profiles were evenly interpreted to 10 m resolution in vertical by applying a cubic spline interpolation. In addition, the sounding with the burst height lower than 10 km above ground level (a.g.l.) was directly discarded for further study. Meteorological variables, including temperature and wind speed, were prepared for the Ri estimation.

One of the shortages of radiosonde measurements is its inadequate concentration over the polar and ocean regions (Xia et al., 2021). The geographical distribution of total profile number of each radiosonde station is demonstrated in Figure S1 in the supporting information. The released radiosoundings over Europe, the United States, and Australia have good geographical coverages and time durations. Over some islands

173 ~~of~~in oceans (e.g., the Pacific Ocean) there are dozens of stations that can provide high-
174 resolution measurements. ~~In~~Over the polar regions, there are around thirty stations.

175 **2.2 ERA5 reanalysis and the collocation procedure**

176 ERA5 is the latest version of ECMWF meteorological reanalysis, benefiting from
177 a decade of developments in model physics, core dynamics, and data assimilation
178 (Hersbach et al., 2020). The wind and temperature fields are modelled by the ERA5
179 reanalysis on a spatial resolution of 0.25° latitude/longitude and a temporal resolution
180 of 1 hour. The reanalysis has 137 model levels, giving a vertical resolution of
181 approximately 300 m in the middle and upper troposphere. The vertical resolution of
182 ERA5 is illustrated in Figure S2. Compared to ERA5, the HVRRS does not provide
183 global seamless observations. Thus, the collocation procedure between reanalysis and
184 HVRRS goes as follows: (1) the matched grid of ERA5 reanalysis is the nearest
185 neighbor of radiosonde station; (2) the regular synoptic start time of radiosonde and
186 reanalysis needs to keep exact the same; (3) the model level of reanalysis that follows
187 a hybrid sigma-pressure coordinate, is converted into geopotential height to match with
188 HVRRS.

189 In addition, the standard deviations of orography (SDOR) and the gravity wave
190 dissipation due to the effects of stress associated with unresolved valleys, hills and
191 mountains in ERA5 reanalysis are extracted.

192 The relative error between HVRRS-based and ERA5-based quantities is estimated
193 by the ratio of deviations between HVRRS and ERA5 derived quantities to the HVRRS
194 one.

195 **2.3 The occurrence frequency of subcritical Ri and its uncertainty**

196 Based on a linear theory, the threshold Ri (Ri_t) defines the ~~threshold~~boundary
197 where the air flow changes from stability to turbulence, and it is usually suggested to
198 be 1/4 (Haack et al., 2014). Ri is formulated as:

$$199 \quad Ri = \bar{N}^2 / \bar{S}^2 \quad (1)$$

200 where N is the Brunt-Väisälä frequency ($\sqrt{\frac{g}{\theta} \frac{d\theta}{dz}}$), S is the vertical ~~wind~~-shear of
 201 horizontal wind ($\sqrt{(\frac{dU}{dz})^2 + (\frac{dV}{dz})^2}$), and the overbar denotes a moving average in a 200
 202 -m bin to eliminate the influence of measurement noises and small-scale fluctuations,
 203 such as turbulence and small-scale waves. Therefore, the wind shear and Brunt-Väisälä
 204 frequency are computed at 10 m resolution, and then those estimates are averaged over
 205 200 m (20 points) and squared. More exactly~~For a vertical resolution of 10 m~~, the
 206 averaged parameter at altitude i can be represented as $\bar{A}(i) = \frac{1}{n} \sum_{j=i-10}^{i+10} A(j)$, where A
 207 denotes wind shear or Brunt-Väisälä frequency and n is the number of vertical bin. In
 208 addition, horizontal winds measured under radiosonde at the scale of a few tens of
 209 meters are affected by the chaotic movements of the gondola due to the pendulum and
 210 to the balloon's own movements (Ingleby et al., 2022). However, it is hard to quantify
 211 ~~the those~~ movements in present study.

212 The Richardson number calculated from Eq.(1) depends on the vertical resolution
 213 of the underlying data, as well as on the averaging interval. Ultimately, this influences
 214 the estimated occurrence frequency for subcritical Richardson numbers as a proxy for
 215 KHI. We resample the HRRRS data to 50 m and 100 m, and range the length scale of
 216 overbar from 100 m to 500 m, to diagnose the uncertainties raised by the length scale
 217 of segments and the vertical resolution of dataset. As indicated in Figure 1, under the
 218 same length scale of overbar, a sparser vertical grid inevitably leads to a lower
 219 occurrence frequency of subcritical Ri . For instance, as the length scale set to 100 m,
 220 the occurrence frequency of $Ri < 1/4$ at 0–2 km above sea level (a.s.l.) decreases from
 221 22% when vertical resolution is equal to 10 m to 16% for a vertical resolution of 50 m.
 222 Moreover, a longer length-scale of segment generally yields a smaller occurrence
 223 frequency. For example, as the vertical resolution of radiosonde is equal to 10 m, the
 224 occurrence frequency at 10–15 km a.s.l. decreases from 9% when the length scale of
 225 segment equals 100 m to 1% when it equals 500 m. It is interesting to note that the
 226 occurrence frequency under a vertical resolution of 50 m and a segment interval of 100
 227 m is a bit larger than that under a vertical resolution of 10 m and a segment of 200 m,
 228 possibly implying ~~the fact~~ that a shorter segment interval could be expected for a sparser

229 vertical resolution.

230 2.4 Gravity wave energy

231 The GW energy is extracted based on the broad spectral method, according to Wang
232 and Geller (2003). In this method, ~~the magnitude of measured~~ zonal wind (u),
233 meridional wind (v), and temperature (T) consist ~~ing~~ of background states (u_0 , v_0 and
234 T_0) that are determined by applying a second-order polynomial fit (Chen et al., 2018;
235 Zhang et al., 2022) and perturbations. Therefore, total perturbations are derived as:

$$236 \quad (u', v', T') = (u, v, T) - (u_0, v_0, T_0) \quad (2)$$

237 The perturbations ~~could~~ include measurement noises, KH waves, GWs, and
238 planetary waves. Only the perturbations with vertical wavelengths of 0.3–6.9 km are
239 considered as GWs (Wang and Geller, 2003). The mean vertical wavelength of GWs is
240 about 2 km (Wang et al., 2005), and therefore, the lowermost threshold of 0.3 km could
241 have limited little influence on the GW energy. However, the retrieval of the largest
242 wavelength is not well determined, which is acknowledged as the radiosonde's
243 “observational filter” (Alexander, 1998). By applying this band-pass filter, the average
244 gravity-wave kinetic energy per unit mass (energy density) and the average potential
245 energy density can be expressed as:

$$246 \quad E_k = \frac{1}{2} [\overline{u'^2} + \overline{v'^2}] \quad (3)$$

$$247 \quad E_p = \frac{1}{2} \frac{g^2 \overline{\hat{T}'^2}}{N^2} \quad (4)$$

248 where g is the gravitational constant, $\hat{T}' = T'/\bar{T}$ the normalized ~~perturbation~~
249 temperature perturbation, and the overbar indicates an averaging over the tropospheric
250 segment, which is chosen as 2–8.9 km for all regions ~~s~~ except the polar region, and it is
251 selected as 2–7.4 km ~~for in~~ the polar region (Wang and Geller, 2003). Eventually, the
252 total GW energy E_t is the sum of E_k and E_p .

253 **3 Results and Discussions**

254 **3.1 Comparisons of wind shear between HVRRS and ERA5 reanalysis**

255 The variations in vertical shear of horizontal wind speed and the squared Brunt-
256 väisälä frequency entirely determine the Ri magnitude. Figure 2 provides an overview
257 of the spatial distribution of wind shear at heights of 0–2 km a.g.l. and 10–15 km a.g.l.
258 obtained from the HVRRS and ERA5 reanalysis. HVRRS-based wind shears are
259 taken from Eq.(1), with a vertical resolution of 10_-m. The ERA5--derived shear at
260 heights of 0–2 km a.g.l. estimated by ERA5 reanalysis demonstrates a strong spatial
261 variation, and it is largely--clearly dependent on underlying terrains and latitudes
262 (Fig.2a). For example, large values can most likely be observed along the coastline,
263 which could be attributed to the prevailing sea-breeze circulation. As compared to the
264 HVRRS, these shears are slightly underestimated by 3.30 m/s/km, based on all
265 sounding measurements (Fig.2b). Nevertheless, a close association between averaged
266 ERA5-reterived shears and HVRRS-determined shears can be noticed in terms of
267 geospatial distribution, with a correlation coefficient of 0.48 (Fig. 2b).

268 It is noteworthy that shears in the ERA5 reanalysis at heights of 10–15 km a.g.l. is
269 are significantly--substantially underestimated compared to the HVRRS, especially at
270 middle latitudes, with a mean absolute error for all stations of about 8 m/s/km (Table
271 1). The underestimation could partly be due to the coarse vertical resolution (around
272 300_-m) in the ERA5 reanalysis in this height interval. HoweverNevertheless, the
273 spatial--geographical distribution of the ERA5 shear still exhibits a significant positive
274 correlation with the HVRRS shear, with a correlation coefficient of 0.44 (Fig.2d).

275 Following Houchi et al. (2010), the monthly averaged shears over seven typical
276 climate zones are separately investigated (Fig. 3), which are defined as follows: polar
277 (70 °–90 °), mid latitudes (40 °–70 °), subtropics (20 °–40 °), and tropics (20 °S–20 °N).
278 Over the polar region in the Northern/Southern Hemisphere, HVRRS-based shears are
279 exceptionally strong in the lower stratosphere compared to those in the troposphere
280 (Fig.3a, g), which could be attributed to the stratospheric polar jet. However, the similar

281 altitude variation can hardly be found in ERA5-based shears that are dramatically
282 underestimated by around 12 m/s/km in the lower stratosphere (Fig.3h, n, also seen in
283 Table 1). The results in midlatitudes reach a similar conclusion (Fig.3b, f, i, m). ~~Over~~
284 In the subtropical regions, HVRRS-based shears are consistent strong at heights of 16–
285 21 km a.g.l., just above the subtropical jet stream (Fig.3c, e). However, in the ERA5
286 reanalysis, the region with consistently strong shears can be noticed at approximately
287 16 km a.g.l. (Fig.3j, l), which is about 3 km lower than that in the HVRRS. One possible
288 reason might be that the model fails to resolve the further increasing shear in the lower
289 stratosphere. In the tropics, the signature of quasi-biennial oscillation (QBO) can be
290 identified in the lower stratosphere (Fig.3d, k).

291 The comparison between HVRRS-based and ERA5-based shears at three typical
292 regimes is tabulated in Table 1. These metrics highlight that ERA5-based shears are
293 underestimated by approximately 3.92 m/s/km, 7.65 m/s/km, 11.99 m/s/km at heights
294 of 0–2 km, 10–15 km, and 20–25 km a.g.l., respectively, which are roughly consistent
295 with Houchi et al. (2010).

296 By comparison, the ERA5-acquired N^2 averaged over four height intervals (e.g.,
297 0–5, 5–10, 10–15, 15–20 km a.g.l.) is reliably estimated ~~at all heights~~, with a relative
298 error of around 11%, as illustrated in Figure S3. This finding indicates that the ERA5
299 reanalysis can properly present the static stability of the background atmosphere, but it
300 is not properly coincident with radiosonde in terms of the small-scale variability of
301 dynamical structures. Due to a lack of global measurement of the fine-structure of the
302 upper-air wind, however, the accuracy of ERA5-resolved shears is hard to be globally
303 validated.

304 **3.2 Occurrence frequency of $Ri < 1/4$ in HVRRS and ERA5 reanalysis**

305 As a prominent example, the monthly occurrence frequency of $Ri < 1/4$ over the
306 Corpus Christi station (27.77° N, –97.5° W) during years from January 2017 to
307 October 2022 is illustrated in Figure 4. As a result, the monthly occurrence rate of
308 $Ri < 1/4$ in the low troposphere determined from HVRRS is lower than the ERA5-based

309 one, with mean values of around 10.6% and 16.9%, respectively. In the lowermost 2
310 km, the vertical resolution of ERA5 reanalysis is less than 200 m, and it is less than the
311 moving segment interval in Eq.(1). The high occurrence frequency in the low
312 troposphere could be likely related to the negative or small N^2 . Especially during the
313 daytime, the planetary boundary layer (PBL) is well mixed due to strong turbulence
314 induced by uprising thermals (Song et al., 2018). In addition, an obvious seasonal cycle
315 of occurrence frequencies is revealed by HVRRS in the middle and upper troposphere
316 and has a maximum in winter (December–January–February) and spring (March–
317 April–May) seasons, which is consistent with the finding in Zhang et al. (2019). In the
318 vicinity of jet streams, the occurrence frequency of $Ri < 1/4$ is generally enhanced by
319 large wind shears. However, the ERA5 reanalysis does not provide such a seasonal
320 cycle pattern, and the occurrence frequency of $Ri < 1/4$ is significantly underestimated
321 by around 8% (Fig.4b), which could be attributed to the underestimation in wind shears.
322 In the lower stratosphere, both the HVRRS and ERA5 reanalysis provide a low
323 estimation of occurrence frequencies, with a value of around 1%.

324 Furthermore, on a large spatial-geographical scale the occurrence frequency of
325 $Ri < 1/4$ retrieved by ERA5 reanalysis is remarkably underestimated in the free
326 atmosphere, as compared to the HVRRS. The annual variation of the occurrence
327 frequency of $Ri < 1/4$ over seven climate zones at 10–15 km a.g.l. indicated by HVRRS
328 and ERA5 reanalysis is further demonstrated in Figure 5. It is clearly seen that the
329 occurrence frequency of $Ri < 1/4$ provided by ERA5 reanalysis is underestimated in all
330 months, over all climate zones, possibly implying that, in the free atmosphere, the
331 threshold value of $1/4$ in Eq.(1) is too small for the ERA5 reanalysis to capture the
332 occurrence of KHI.

333 However, the ERA5 reanalysis data is non-uniformly sampled in altitude. Its
334 vertical resolution drops from about 100_-m in the boundary layer to about 500_-m in
335 the lower stratosphere. In contrast, radiosondes have a vertical resolution of 10_-m at
336 all heights. Therefore, we selected four typical heights and vertically interpolated the
337 radiosonde to the same height resolution as ERA5 for comparison. The four height
338 intervals are 0.8–1.3 km, 2.2–3.2 km, 6–15 km and 20–21 km a.g.l., as shown in Table

339 2. In these height intervals, the vertical resolution of ERA5 is about 100_-m, 200_-m,
340 300_-m and 400_-m respectively. Even at the same vertical resolution, ERA5 still
341 seriously underestimates the value of $OF(Ri < 1/4)$ at all heights and ~~all~~ climate zones.
342 These results indicate that the greatest difficulty in evaluating subcritical Ri with ERA5
343 is that its simulation of wind shears might be seriously underestimated compared with
344 radiosonde. As illustrated in Table 3, even accounting for the fact that ERA5 has a
345 comparable vertical resolution ~~as the~~ radiosonde, wind shears in ERA5 reanalysis are
346 still underestimated by around 50.3%, 48.7%, 43.6%, and 62.2% at 0.8–1.3 km, 2.2–
347 3.2 km, 6–15 km and 20–21 km a.g.l., respectively. In order to obtain an occurrence
348 frequency of subcritical Ri from ERA5 reanalysis that is comparable with radiosonde-
349 based $OF(Ri < 1/4)$, the Rit for ERA5 should be set larger than 1/4. For instance, at 0.8–
350 1.3 km and 2.2–3.2 km a.g.l., the Rit equals 1 could be a proper choice for ERA5
351 reanalysis, rather than 1/4 (Table 2). More generally, $0.5 < Rit < 1.5$ could be more
352 suitable for ERA5 reanalysis, compared to $Rit = 1/4$.

353 Due to the huge change in the vertical resolution of ERA5, it could be difficult to
354 interpolate ERA5 into uniform data vertically with a relatively high resolution.
355 Therefore, the question posed here is, what is the proper threshold value of Ri in
356 predicting the occurrence of KHI when using the ERA5 reanalysis, compared to
357 HVRRS? The occurrence frequency of $Ri < 1/4$ indicated by the HVRRS, the ERA5-
358 determined occurrence frequencies produced by $Ri < 0.25$, $Ri < 0.5$, $Ri < 1$, $Ri < 1.5$, and
359 $Ri < 2$ at all heights up to 30 km a.g.l. are demonstrated in Figure 6. It is notable that
360 over all climate zones and in the free atmosphere, occurrence frequencies of $Ri < 0.25$
361 and $Ri < 0.5$ obtained from the ERA5 reanalysis are underestimated, but the frequencies
362 of $Ri < 1.5$ and $Ri < 2$ are generally overestimated. The occurrence frequency of $Ri < 1$
363 gives a close estimation both in magnitude and ~~altitudespatial~~ variations compared to
364 HVRRS over all climate zones.

365 Furthermore, the correlation coefficients between HVRRS-determined
366 occurrence frequencies and the ERA5-determined frequencies indicated by different
367 threshold values of Ri at height levels of 0 to 30 km are illustrated in Figure 7. It is
368 worth noting that, in the troposphere, the ERA5-based frequencies indicated by $Ri < 1$,

369 $Ri < 1.5$, and $Ri < 2$ are highly positively correlated with those from the HVRRS, with a
370 correlation coefficient of around 0.6 over all climate zones. In the lower stratosphere,
371 however, these coefficients rapidly decline to 0.1, which can be explained by the low
372 occurrence frequency in this height regime.

373 Combined the findings in Figures 6 and 7, in the free troposphere, we can conclude
374 that the ERA5-determined occurrence frequency of $Ri < 1$ is closest to the frequency of
375 $Ri < 1/4$ based on the HVRRS. In the free atmosphere, KHI is the dominant source for
376 clear-air turbulence (CAT) that is a well-known hazard to aviation. Therefore, the global
377 characterization of KHI occurrence frequency in the free atmosphere obtained from
378 ERA5 reanalysis could be of importance for understanding the spatial-temporal
379 variation of CAT. In the following sections, the occurrence frequency of subcritical Ri
380 (hereinafter $OF(Ri < Rit)$) is based on $Ri < 1$ in ERA5 reanalysis and $Ri < 1/4$ in HVRRS,
381 unless otherwise noted.

382 Finally, it is noteworthy that $OF(Ri < Rit)$ includes the component of $Ri < 0$ that
383 indicates potential for convective instability. However, both ERA5 and HVRRS are
384 difficult to totally avoid $Ri < 0$ when calculating Ri . Therefore, we evaluated the
385 proportion of $Ri < 0$ in all $Ri < Rit$ ~~across in the~~ two datasets to evaluate the possible
386 contribution from convections, as shown in Figure 8. For HVRRS, the proportion of
387 $OF(Ri < 0)$ drops sharply from about 40% in the low troposphere to about 18% at 5–15
388 km a.g.l.. Similarly, for ERA5 its proportion drops from about 40% in the lowermost
389 part of the atmosphere to about 2% at 5–16 km a.g.l.. These findings indicate that, in
390 the free atmosphere, $OF(Ri < Rit)$ is mainly composed of $OF(0 < Ri < Rit)$, ~~which implies~~
391 ~~that local instabilities constitute most of the dynamic instability.~~

392 3.3 The $OF(Ri < Rit)$ climatology

393 For a first hint, the global distributions of $OF(Ri < Rit)$ provided by the ERA5
394 reanalysis at 0–2 km, 5–10 km, 10–15 km, and 15–20 km a.g.l. are displayed in Figure
395 9. $OF(Ri < Rit)$ in the low troposphere is considerably spatially heterogeneous. ~~Over In~~
396 ~~subtropical oceans in the Northern/Southern Hemisphere,~~ the intense $OF(Ri < Rit)$ can

397 be noticed and has a magnitude of around 50% (Fig.9a). In addition, ~~over-in~~ the Sahara
398 Desert the $OF(Ri < Rit)$ reaches as high as 65%. Interestingly, the spatial variation in
399 ~~mean~~ $OF(Ri < Rit)$ ~~enssembled by y~~during years 2017–2022 keeps high consistency
400 with that of planetary boundary layer height (PBLH) over oceans, such as the Pacific
401 Ocean near Japan and the Atlantic Ocean near U.S., as shown in Figure S4. However,
402 at 0–2 km a.g.l., the spatial variation of $OF(0 < Ri < Rit)$ exhibits a large difference with
403 that of $OF(Ri < Rit)$ in terms of magnitude, as shown in Figure S5. It is around 40%
404 (20%) lower than that of $OF(Ri < Rit)$ ~~over-in~~ subtropical oceans (Australia and North
405 Africa). At heights of 5–10 km a.g.l., intensive $OF(Ri < Rit)$ can be viewed ~~over-in~~ the
406 ~~subtropie-subtropical~~ regions and has a value of around 10% (Fig.9b), which is likely
407 attributed to upper tropospheric jets. —In the upper troposphere ~~over-above~~ the
408 tropical oceans, $OF(Ri < Rit)$ is as high as 30% (Fig.9c), possibly as a result of the
409 maximal heating effect by mesoscale convective systems (e.g., Houze 1982). In the
410 lower stratosphere, $OF(Ri < Rit)$ sharply decreases to around 0.1% (Fig.9d).

411 In comparison, the spatial-temporal variability of free-tropospheric $OF(Ri < Rit)$
412 indicated by HVRRS ~~keeps-is fairly~~highly consistentey with that of ERA5 reanalysis
413 over all climate zones ~~and in the free troposphere, except in the stratosphere of polar~~
414 ~~region~~ (Figure 10). Seasonal cycles can be detected by both the HVRRS and ERA5
415 reanalysis over all climate zones, especially ~~over-in the~~ subtropics and midlatitudes
416 ~~regions~~. However, the ERA5-based $-OF(Ri < Rit)$ can only reflect the large scale
417 structure of the cycles, and it is hard to quantify the detailed variation like the HVRRS
418 does.

419 Furthermore, the seasonal variation of $OF(Ri < Rit)$ with $Rit=1/4$ for HVRRS and
420 $Rit=1$ for ERA5 ~~infor~~ all climate zones is further ~~analyzed-provided~~ in Figure 11. In the
421 midlatitudes and subtropics, the $OF(Ri < Rit)$ exhibits maximum values in the low
422 troposphere, as well as a local minimum in the middle troposphere and a local
423 maximum at altitudes around 9 km. In the lower stratosphere, the occurrence
424 frequencies decrease to values of the order of 1% (Fig.11b,c,e,f). ~~Over-In~~ tropics
425 ~~regions~~, a primary peak can be clearly noticed at around 13 km, with a maximum of
426 12% for the HVRRS and 20% for the ERA5 reanalysis (Fig.11d, k). The seasonality

427 ~~over~~ in the tropical region could be related to some large scale flow features like the
428 Summer Asian Monsoon and the tropical easterly jet (Roja Raman et al., 2009;
429 Sunilkumar et al., 2015; Kaluza et al., 2021). ~~Over~~ In polar regions, the tropospheric
430 $OF(Ri < Rit)$ is significantly lower than that ~~of~~ over other climate zones, with values
431 ranging from around 4% at heights of 2–8 km to 1% in the lower stratosphere
432 (Fig.11a,g).

433 In Table 4, the mean $OF(Ri < Rit)$ magnitudes over seven climate zones and at three
434 typical altitude regimes are listed. At 0–2 km a.g.l., the ERA5-based $OF(Ri < Rit)$ is
435 about 24% larger than that of the HVRRS-based one. At 10–15 km a.g.l., the ERA5-
436 based $OF(Ri < Rit)$ is reasonably well estimated, except that it is overestimated by
437 around 5.92% ~~in tropic~~ over the tropics region. In addition, ERA5 underestimates
438 $OF(Ri < Rit)$ by around 0.5% in the lower stratosphere.

439 According to Fig.9a, it seems that low-level continental $OF(Ri < Rit)$ is dependent
440 on underlying terrains. We investigate the association of low-level HVRRS-determined
441 $OF(Ri < Rit)$ with the standard deviation of orography (SDOR). At heights of 1–2 km
442 a.g.l., the underlying terrain with a large SDOR generally corresponds to a high
443 $OF(Ri < Rit)$, with a correlation coefficient between $OF(Ri < Rit)$ and SDOR of 0.24.
444 Then, the coefficient decreases to 0.15 at 3–4 km a.g.l. (Fig.12b), and eventually, it
445 equals 0.14 at 5–6 km a.g.l. (Fig.12c). These findings indicate that ~~the~~ complex terrain
446 may locally enhance $OF(Ri < Rit)$.

447 Moreover, it is quite evident from Fig.9b and Fig.S5 that both $OF(Ri < Rit)$ and
448 $OF(0 < Ri < Rit)$ are largely enhanced ~~over~~ above the tropical ocean associated with the
449 El Niño Southern Oscillation (ENSO). The most of the enhanced $OF(Ri < Rit)$ can be
450 identified over the Niño 3 region (5 °N–5 °S, 150 °W–90 °W), and the time-height cross
451 section of $OF(Ri < Rit)$ during years ~~of 2000 to~~ 2000–2022 is illustrated in Figure 13. The
452 $OF(Ri < Rit)$ at height region of 6–13 km are evidently large, with values of around 35%,
453 which is about 15% larger than the climatological mean value (Fig.10k). More
454 specifically, $OF(Ri < Rit)$ during time periods of La Niña events is obviously stronger
455 than that during the El Niño periods. The identification of ENSO events is based on
456 Ren et al. (2018), Li et al. (2022), and Lv et al. (2022). It is also worth recalling here

457 that the wind shear does not exhibit such an anomaly over the Niño 3 region (Fig.2c),
458 implying that the $OF(Ri < Rit)$ anomaly could likely be attributed to the ENSO-related
459 tropical convective heating in the upper troposphere, leading to a low Brunt-Väisälä
460 frequency.

461 3.4 The dynamical environment of $OF(Ri < Rit)$ in the free troposphere

462 In the free troposphere the percentage of $OF(Ri < 0)$ relative to $OF(Ri < Rit)$ is
463 generally less than 20% (Fig. 8), KHI is preferentially generated from strong wind
464 shears, which may be closely associated with mean flows and wave activities.

465 The propagation of GW could raise strong wind shear, and therefore generate KHI.
466 Thereby, we investigate the joint distribution of $OF(Ri < Rit)$ with tropospheric GW total
467 energy and wind shear (Figure 14). The latitudinal variation of GW total energy exhibits
468 a double-peak structure, with two peaks at around 30° in the Northern/Southern
469 Hemisphere (Fig.14a). The joint distribution of $OF(Ri < Rit)$ with GW energy and wind
470 shear indicates that large $OF(Ri < Rit)$ (for instance, ~~>larger than~~10%) generally
471 corresponds to GW energy larger than 10 J/kg or wind shear exceeds 14 m/s/km (Fig.
472 14b). Also, $OF(0 < Ri < Rit)$ exhibits a similar distribution (Figure S6). Overall,
473 $OF(Ri < Rit)$ obviously increases with GW total energy (Figure S9a), possibly implying
474 that the propagation of GWs could enhance wind shears and therefore, the burst of KHI.

475 In addition, the interaction between low-level winds and mountain barriers could
476 be a source of orographic GWs (Zhang et al., 2022). We take orographic GW dissipation
477 in ERA5 reanalysis, which is the accumulated conversion of kinetic energy in the mean
478 flow into heat over the whole atmospheric column, as an indicator of the strength of
479 orographic GWs. It is interesting to note that monthly averaged orographic GW
480 dissipation and monthly ERA5-determined $OF(Ri < Rit)$ at heights from ~~near-~~
481 ~~groundground~~ up to 30 km demonstrates a close association (Figure S7). For instance,
482 in the middle troposphere, they are positively associated over mountainous areas such
483 as the Rocky Mountains and the Alps Mountain, with correlation coefficients of around
484 0.5. These findings also suggest that during months with strong unresolved orographic

485 gravity wave activity, which then modify the flow and stability parameters of the
486 resolved flow, leading to a low Richardson number. Nevertheless, it is hard to quantify
487 the effect of resolved orographic GWs on Ri here.

488 At jet heights (10–15 km a.g.l.), a large shear can be easily induced by strong wind
489 speeds. Figure 15 demonstrates the joint distribution of $OF(Ri < Rit)$ with wind speed
490 and wind shear. Generally, $OF(Ri < Rit)$ larger than 10% can be easily found when the
491 wind shear exceeds 20 m/s/km. In addition, $OF(0 < Ri < Rit)$ draws a similar conclusion
492 (Figure S8). In the middle and upper troposphere, $OF(Ri < Rit)$ almost linearly increases
493 with wind speed (Figure S9b).

494 In a short conclusion, in the free troposphere, the occurrence of KHI would favor
495 the dynamical environment with intensive orographic or non-orographic GW activities
496 and large mean flows.

497 **4 Conclusion and remarks**

498 The occurrence of KHI is potential crucial for many implications, such as aircraft
499 safety and mass transfer, but it is very hard to be globally understood due to its fine
500 structure. The subcritical Richardson number is commonly used as an indicator for KHI.
501 This study uses the ERA5 as the latest reanalysis product from the ECMWF as well as
502 a comprehensive data-set of HVRRS-high-resolution radiosonde soundings to globally
503 characterize the distribution of low Richardson numbers as a proxy for the occurrence
504 of KHI, for the years 2017 to 2022.

505 Vertical wind shears are considerably underestimated at almost all heights and over
506 all climate zones by the ERA5 reanalysis, compared to the HVRRS. It is noteworthy
507 that vertical wind shear in the ERA5 reanalysis at heights of 10–15 km a.g.l. is
508 dramatically underestimated by around 7.65 m/s/km, especially at middle latitudes.
509 However, the spatial distribution of the ERA5 shear exhibits a statistically significant
510 positive correlation with the HVRRS shear. As a result, the ERA5-determined
511 occurrence frequency of $Ri < 1/4$ is significantly underestimated. In addition, it is weak
512 correlated with HVRRS-determined ones at most heights and over most climate zones.

513 However, the vertical resolution of ERA5 reanalysis sharply decreases with altitude,
514 which is not comparable with HVRRS. Thus, to match with ERA5 reanalysis at
515 specified height intervals, the HVRRS was vertically interpolated with resolutions
516 spanning from 100_-m to 400_-m. Even at a comparable resolution, ERA5-derived
517 ~~vertical wind~~-shear is underestimated by around 50%, leading to a considerable
518 underestimation in $OF(Ri < 1/4)$, compared to radiosondes.

519 Interestingly, the ERA5-determined occurrence frequency of $Ri < 1$ is generally
520 consistent with the frequency of $Ri < 1/4$ obtained from HVRRS, in terms of magnitude
521 and temporal variation. Rather than $Ri < 1/4$, we argue that the threshold value of $Ri < 1$
522 could be more proper when using ERA5 reanalysis for KHI study, especially in the
523 middle and upper troposphere over midlatitude and subtropic regions in the
524 Northern/Southern Hemisphere, where a high consistency between HVRRS and ERA5
525 has been found in terms of $OF(Ri < Rit)$ magnitude. In other words, under a similar
526 occurrence frequency, the identification of vertical segments with $Ri < 1$ in ERA5 is
527 equitable with identification of vertical segments with $Ri < 1/4$ using HVRRS. It is worth
528 highlighting that HVRRS experiences a 200_-m vertical moving average procedure to
529 inhabit measurement noises and turbulence fluctuations. Without this procedure, the
530 threshold Ri for the ERA5 reanalysis would even higher than 1.

531 The climatology of $OF(Ri < Rit)$ exhibits significant seasonal cycles over all
532 latitudes. A poleward decrease can be clearly identified in the middle and upper
533 troposphere. In addition, over mountainous areas, complex terrains may locally
534 enhance low-level $OF(Ri < Rit)$. Moreover, it is immediately obvious that the both
535 $OF(Ri < Rit)$ and $OF(0 < Ri < Rit)$ in the middle and upper troposphere of the Niño 3 region
536 is largely-considerably enhanced probably by the tropical convective heating.

537 Moreover, both $OF(Ri < Rit)$ and $OF(0 < Ri < Rit)$ exhibit close relationship with GW
538 activities and background mean flows. For instance, Large $OF(Ri < Rit)$ favors intensive
539 GW activities and strong mean flow. Over complex terrains, the orographic GW
540 breaking could locally enhance $OF(Ri < Rit)$.

541 Those findings are valuable for pointing out the performance of the ERA5
542 reanalysis in terms of resolving low Richardson numbers as a proxy for KHI, in

543 comparison with a near-global high-resolution radiosonde measurement. In addition,
544 the spatial-temporal variability of $OF(Ri < Rit)$ over different climate zones from near-
545 ground up to 30 km is quantitatively characterized by ERA5 and HVRRS, which could
546 provide new insights that increase our understanding of the fine structure of upper air.
547

548 **Acknowledgement**

549 The authors would like to acknowledge the National Meteorological Information
550 Centre (NMIC) of CMA, NOAA, Deutscher Wetterdienst (Climate Data Center), U.K
551 Centre for Environmental Data Analysis (CEDA), GRUAN, ECMWF, and the
552 University of Wyoming for continuously collecting and generously providing high-
553 resolution radiosonde data. Last but not least, we would like to thank two anonymous
554 reviewers for their excellent comments that greatly helped to improve our work.

555

556 **Financial support**

557 This study jointly supported by the National Natural Science Foundation of China under
558 grants 42205074, 62101203 and 42127805, the Hubei Provincial Natural Science
559 Foundation of China under Grant 2021CFB459, and the Research Grants of Huazhong
560 Agricultural University under grants No. 2662021XXQD002 and 2662021JC008.

561

562 **Competing interests**

563 The contact author has declared that neither they nor their co-authors have any
564 competing interests

565

566 **Data availability**

567 The dataset can be accessed at ECMWF (2022).

568

569 **Author contributions**

570 JZ conceptualized this study. JS and JZ carried out the analysis with comments from
571 other co-authors. JZ wrote the original manuscript. WW, SZ, TY, WD provided useful
572 suggestions for the study. All authors contributed to the improvement of paper.

573

574 **References**

575 Alexander, M. J.: Interpretations of observed climatological patterns in stratospheric
576 gravity wave variance, *J. Geophys. Res. Atmos.*, 103(D8), 8627–8640,
577 <https://doi.org/10.1029/97JD03325>, 1998.

578 Duruisseau, F., N., Huret, A., Andral, and Camy-Peyret, C.: Assessment of the ERA-
579 Interim winds using high-altitude stratospheric balloons, *J. Atmos. Sci.*, 74(6),
580 2065–2080, <https://doi.org/10.1175/JAS-D-16-0137.1>, 2017.

581 ECMWF: ECMWF Reanalysis v5 (ERA5), European Centre for Medium-Range
582 Weather Forecasts [data set],
583 <https://www.ecmwf.int/en/forecasts/dataset/ecmwf-reanalysis-v5>, last access:
584 07 December 2022.

585 Fritts, D. C., K. Wan, J. Werne, T. Lund, and Hecht, J. H.: Modeling the implications of
586 Kelvin-Helmholtz instability dynamics for airglow observations, *J. Geophys.*
587 *Res. Atmos.*, 119, 8858–8871, <https://doi.org/10.1002/2014JD021737>, 2014.

588 Fritts, D. C., P. M. Franke, K. Wan, T. Lund, and Werne, J.: Computation of clear-air
589 radar backscatter from numerical simulations of turbulence: 2. Backscatter
590 moments throughout the lifecycle of a Kelvin Helmholtz instability, *J. Geophys.*

591 Res., 116, D11105, <https://doi.org/10.1029/2010JD014618>, 2011.

592 Fritts, D. C., and Rastogi, P. K.: Convective and dynamical instabilities due to gravity
593 wave motions in the lower and middle atmosphere: Theory and observations.
594 Radio Sci., 20, 1247–1277, <https://doi.org/10.1029/RS020i006p01247>, 1985.

595 Fritts, D. C., L., Wang, T. S., Lund, S. A., Thorpe, C. B., Kjellstrand, B., Kaifler, and
596 Kaifler, N.: Multi-Scale Kelvin-Helmholtz instability dynamics observed by
597 PMC Turbo on 12 July 2018: 2. DNS modeling of KHI dynamics and PMC
598 responses., J. Geophys. Res. Atmos., 127, e2021JD035834.
599 <https://doi.org/10.1029/2021JD035834>, 2022.

600 Grasmick, C., and Geerts, B.: Detailed dual-Doppler structure of Kelvin–Helmholtz
601 waves from an airborne profiling radar over complex terrain. Part I: Dynamic
602 structure, J. Atmos. Sci., 77(5), 1761–1782., [https://doi.org/10.1175/JAS-D-19-](https://doi.org/10.1175/JAS-D-19-0108.1)
603 0108.1, 2020.

604 Gavrilov, N. M., Luce, H., Crochet, M., Dalaudier, F., and Fukao, S.: Turbulence
605 parameter estimations from high-resolution balloon temperature measurements
606 of the MUTSI-2000 campaign, Ann. Geophys., 23, 2401–2413,
607 doi:10.5194/angeo-23-2401-2005, 2005

608 Gu, L., Yin, J., Gentine, P. et al.: Large anomalies in future extreme precipitation
609 sensitivity driven by atmospheric dynamics, Nat. Commun., 14, 3197,
610 <https://doi.org/10.1038/s41467-023-39039-7>, 2023

611 Guo, J., Zhang, J., Yang, K., Liao, H., Zhang, S., Huang, K., Lv, Y., Shao, J., Yu, T.,
612 Tong, B., Li, J., Su, T., Yim, S. H. L., Stoffelen, A., Zhai, P., and Xu, X.:
613 Investigation of near-global daytime boundary layer height using high-
614 resolution radiosondes: first results and comparison with ERA5, MERRA-2,
615 JRA-55, and NCEP-2 reanalyses, Atmos. Chem. Phys., 21, 17079–17097,
616 <https://doi.org/10.5194/acp-21-17079-2021>, 2021.

617 Haack, A., M. Gerding, and Lübken, F.-J.: Characteristics of stratospheric turbulent
618 layers measured by LITOS and their relation to the Richardson number, J.
619 Geophys. Res. Atmos., 119, 10605–10618,
620 <https://doi.org/10.1002/2013JD021008>, 2014.

621 Hersbach, H., Bell, B., Berrisford, P., Hirahara, S., Horányi, A., Muñoz-Sabater, J.,
622 Nicolas, J., Peubey, C., Radu, R., Schepers, D., Simmons, A., Soci, C., Abdalla,
623 S., Abellan, X., Balsamo, G., Bechtold, P., Biavati, G., Bidlot, J., Bonavita, M.,
624 De Chiara, G., Dahlgren, P., Dee, D., Diamantakis, M., Dragani, R., Flemming,
625 J., Forbes, R., Fuentes, M., Geer, A., Haimberger, L., Healy, S., Hogan, R. J.,
626 Hólm, E., Janisková, M., Keeley, S., Laloyaux, P., Lopez, P., Lupu, C., Radnoti,
627 G., de Rosnay, P., Rozum, I., Vamborg, F., Villaume, S., and Thépaut, J.-N.: The
628 ERA5 global reanalysis, *Q. J. Roy. Meteorol. Soc.*, 146, 1999–2049,
629 <https://doi.org/10.1002/qj.3803>, 2020.

630 Homeyer, C. R., L. L. Pan, and Barth, M. C.: Transport from convective overshooting
631 of the extratropical tropopause and the role of large-scale lower stratospheric
632 stability, *J. Geophys. Res. Atmos.*, 119(5), 2220–2240,
633 <https://doi.org/10.1002/2013JD020931>, 2014.

634 Houchi, K., Stoffelen, A., Marseille, G. J., and De Kloe, J.: Comparison of wind and
635 wind shear climatologies derived from high-resolution radiosondes and the
636 ECMWF model, *J. Geophys. Res.-Atmos.*, 115, D22123,
637 <https://doi.org/10.1029/2009JD013196>, 2010.

638 Houze, R. A., Jr.: Cloud clusters and large-scale vertical motions in the tropics, *J.*
639 *Meteor. Soc. Japan*, 60, 396–410, https://doi.org/10.2151/jmsj1965.60.1_396,
640 1982.

641 Ingleby, B., Motl, M., Marlton, G., Edwards, D., Sommer, M., von Rohden, C., Vömel,
642 H., and Jauhiainen, H.: On the quality of RS41 radiosonde descent data, *Atmos.*
643 *Meas. Tech.*, 15, 165–183, <https://doi.org/10.5194/amt-15-165-2022>, 2022.

644 Lazarus, S. M., Chiappa, J., Besing, H., Splitt, M. E., and Rioussset, J. A.: Distinguishing
645 characteristics of the tropical cyclone gigantic jet environment, *J. Atmos. Sci.*,
646 78(9), 2741–2761, <https://doi.org/10.1175/JAS-D-20-0265.1>, 2021.

647 Lee, S. H., Williams, P. D., and Frame, T. H.: Increased shear in the North Atlantic
648 upper-level jet stream over the past four decades, *Nature*, 572, 639–642,
649 <https://doi.org/10.1038/s41586-019-1465-z>, 2019.

650 Lee, J. H., Kim, J.-H., Sharman, R. D., Kim, J., and Son, S.-W. Climatology of Clear-

651 Air Turbulence in upper troposphere and lower stratosphere in the Northern
652 Hemisphere using ERA5 reanalysis data, *J. Geophys. Res.-Atmos.*, 128,
653 e2022JD037679, <https://doi.org/10.1029/2022JD037679>, 2023.

654 Li, X., Hu, Z. Z., Tseng, Y. H., Liu, Y., and Liang, P.: A historical perspective of the La
655 Niña event in 2020/2021, *J. Geophys. Res.-Atmos.*, 127(7), e2021JD035546,
656 <https://doi.org/10.1029/2021JD035546>, 2022.

657 Lv, A., Fan, L., and Zhang, W.: Impact of ENSO Events on Droughts in China,
658 *Atmosphere*, 13(11), 1764, <https://doi.org/10.3390/atmos13111764>, 2022.

659 Jaeger, E. B., and Sprenger, M.: A Northern Hemispheric climatology of indices for
660 clear air turbulence in the tropopause region derived from ERA40 reanalysis
661 data, *J. Geophys. Res.*, 112, D20106, doi:10.1029/2006JD008189, 2007.

662 Kaluza, T., Kunkel, D., and Hoor, P.: On the occurrence of strong vertical wind shear
663 in the tropopause region: a 10-year ERA5 northern hemispheric study, *Weather
664 Clim. Dynam.*, 2, 631–651, <https://doi.org/10.5194/wcd-2-631-2021>, 2021.

665 Kunkel, D., Hoor, P., Kaluza, T., Ungermann, J., Kluschat, B., Giez, A., Lachnitt, H.-
666 C., Kaufmann, M., and Riese, M.: Evidence of small-scale quasi-isentropic
667 mixing in ridges of extratropical baroclinic waves, *Atmos. Chem. Phys.*, 19,
668 12607–12630, <https://doi.org/10.5194/acp-19-12607-2019>, 2019.

669 Ko, H. C., H. Y., Chun, R., Wilson, and Geller, M. A.: Characteristics of
670 atmospheric turbulence retrieved from high vertical-resolution radiosonde
671 data in the United States, *J. Geophys. Res. Atmos.*,
672 124, <https://doi.org/10.1029/2019JD030287>, 2019.

673 Ko, H. C. and Chun, H. Y.: Potential sources of atmospheric turbulence estimated using
674 the Thorpe method and operational radiosonde data in the United States. *Atmos.
675 Res.*, 265, 105891, <https://doi.org/10.1016/j.atmosres.2021.105891>, 2022.

676 Muschinski, A., and Wode, C.: First in situ evidence for coexisting submeter
677 temperature and humidity sheets in the lower free troposphere, *J. Atmos. Sci.*,
678 55(18), 2893–2906, [https://doi.org/10.1175/1520-0469\(1998\)055<2893:FISEFC>2.0.CO;2](https://doi.org/10.1175/1520-0469(1998)055<2893:FISEFC>2.0.CO;2), 1998.

680 North, G. R., Pyle, J. A., and Zhang, F.: *Encyclopedia of atmospheric sciences*,

681 Academic Press, Cambridge, Massachusetts, United States, 224 pp., 2014

682 Plougonven, R., and Zhang, F.: Internal gravity waves from atmospheric jets and fronts,
683 *Rev. Geophys.*, 52, 33–76, <https://doi.org/10.1002/2012RG000419>, 2014.

684 Ren, H. L., B., Lu, J., Wan, B., Tian, and Zhang, P.: Identification standard for ENSO
685 events and its application to climate monitoring and prediction in China, *J.*
686 *Meteorol. Res.*, 32, 923–936, <https://doi.org/10.1007/s13351-018-8078-6>, 2018.

687 Roja Raman, M., Jagannadha Rao, V. V., Venkat Ratnam, M., Rajeevan, M., Rao, S. V.,
688 Narayana Rao, D., and Prabhakara Rao, N.: Characteristics of the Tropical
689 Easterly Jet: Long-term trends and their features during active and break
690 monsoon phases, *J. Geophys. Res.-Atmos.*, 114, 1–14,
691 <https://doi.org/10.1029/2009JD012065>, 2009.

692 Sandu, I., A., A., van Niekerk, T. G., Shepherd, S. B., Vosper, A., Zadra, J., Bacmeister,
693 et al: Impacts of orography on large-scale atmospheric circulation. *npj Clim*
694 *Atmos Sci*, 2(1), 1–8, <https://doi.org/10.1038/s41612-019-0065-9>, 2019.

695 Savazzi, A. C. M., Nuijens, L., Sandu, I., George, G., and Bechtold, P.: The
696 representation of the trade winds in ECMWF forecasts and reanalyses during
697 EUREC⁴A, *Atmos. Chem. Phys.*, 22, 13049–13066,
698 <https://doi.org/10.5194/acp-22-13049-2022>, 2022.

699 Sharman, R. D., S. B. Trier, T. P. Lane, and Doyle, J. D.: Sources and dynamics of
700 turbulence in the upper troposphere and lower stratosphere: A review, *Geophys.*
701 *Res. Lett.*, 39, L12803, <https://doi.org/10.1029/2012GL051996>, 2012.

702 Sharman, R. D., and Pearson, J. M: Prediction of energy dissipation rates for aviation
703 turbulence. Part I: Forecasting nonconvective turbulence. *J. Appl. Meteorol.*
704 *Climatol*, 56(2), 317–337, <https://doi.org/10.1175/JAMC-D-16-0205.1>, 2017.

705 Song, J., Z.-H., Wang, and Wang, C.: The regional impact of urban heat mitigation
706 strategies on planetary boundary layer dynamics over a semiarid city, *J.*
707 *Geophys. Res. Atmos.*, 123(12), 6410–6422,
708 <https://doi.org/10.1029/2018JD028302>, 2018.

709 Sunilkumar, S. V., Muhsin, M., Parameswaran, K., Venkat Ratnam, M., Ramkumar,
710 G., Rajeev, K., Krishna Murthy, B. V., Sambhu Namboodiri, K. V.,

711 Subrahmanyam, K. V., Kishore Kumar, K., and Shankar Das, S.: Characteristics
712 of turbulence in the troposphere and lower stratosphere over the Indian
713 Peninsula, *J. Atmos. Sol.-Terr. Phys.*, 133, 36–53,
714 <https://doi.org/10.1016/j.jastp.2015.07.015>, 2015.

715 Wang, L., and Geller, M. A.: Morphology of gravity-wave energy as observed from 4
716 years (1998–2001) of high vertical resolution U.S. radiosonde data, *J. Geophys.*
717 *Res. Atmos.*, 108(D16), 4489, <https://doi.org/10.1029/2002JD002786>, 2003.

718 Wang, L., Geller, M. A., and Alexander, M. J.: Spatial and Temporal Variations of
719 Gravity Wave Parameters, Part I: Intrinsic Frequency, Wavelength, and Vertical
720 Propagation Direction, *J. Atmos. Sci.*, 62, 125–142,
721 <https://doi.org/10.1175/JAS-3364.1>, 2005

722 Williams, P. D., and Joshi, M. M.: Intensification of winter transatlantic aviation
723 turbulence in response to climate change. *Nat. Clim. Chang.*, 3(7), 644–648,
724 <https://doi.org/10.1038/nclimate1866>, 2013.

725 Xia, P., Y., Shan, S., Ye, and Jiang, W.: Identification of Tropopause Height with
726 Atmospheric Refractivity, *J. Atmos. Sci.*, 78(1), 3–16
727 <https://doi.org/10.1175/JAS-D-20-0009.1>, 2021.

728 Zhang, J., S. D., Zhang, C. M., Huang, K. M., Huang, Y., Gong, Q., Gan, and Zhang,
729 Y. H.: Latitudinal and topographical variabilities of free atmospheric turbulence
730 from high-resolution radiosonde data sets, *J. Geophys. Res. Atmos.*, 124, 4283–
731 4298. <https://doi.org/10.1029/2018JD029982>, 2019.

732 Zhang, J., J., Guo, H., Xue, S., Zhang, K., Huang, W. Dong, et al.: Tropospheric gravity
733 waves as observed by the high-resolution China radiosonde network and their
734 potential sources, *J. Geophys. Res. Atmos.*, 127, e2022JD037174,
735 <https://doi.org/10.1029/2022JD037174>, 2022.

736 Zhang, J., J., Guo, S., Zhang, and Shao, J.: Inertia-gravity wave energy and instability
737 drive turbulence: Evidence from a near-global high-resolution radiosonde
738 dataset, *Clim. Dyn.*, 58(11), 2927–2939, [https://doi.org/10.1007/s00382-021-](https://doi.org/10.1007/s00382-021-06075-2)
739 [06075-2](https://doi.org/10.1007/s00382-021-06075-2), 2022.

740

741
742
743
744
745
746
747
748
749
750
751
752
753
754
755
756
757
758

Table 1. Comparisons of mean wind shears between HVRRS and ERA5 reanalysis at heights of 0–2 km a.g.l. (a), 10–15 km a.g.l. (b), and 20–25 km a.g.l. (c).

(a) Wind shear at 0–2 km a.g.l. (m/s/km)							
	Polar	Midlatitude	Subtropics	Tropics	Subtropics	Midlatitude	Polar
	(NH)	(NH)	(NH)		(SH)	(SH)	(SH)
HVRRS	12.60	12.72	12.10	10.64	12.82	14.12	15.35
ERA5	8.02	9.14	8.62	5.21	8.54	10.32	8.73
(b) Wind shear at 10–15 km a.g.l. (m/s/km)							
HVRRS	13.22	14.95	13.38	9.49	13.52	14.66	13.11
ERA5	4.17	6.08	6.76	5.79	6.74	5.13	3.38
(c) Wind shear at 20–25 km a.g.l. (m/s/km)							
HVRRS	15.17	15.66	15.20	16.72	16.57	16.12	17.19
ERA5	2.85	3.48	4.03	5.22	3.92	3.33	2.90

759
760
761
762
763
764
765
766
767
768
769

770 **Table 2.** The occurrence rate of low Ri at 0.8–1.3 km a.g.l. (a), 2.2–3.2 km a.g.l. (b),
771 6–15 km a.g.l. (c), and 20–21 km a.g.l. (d). The critical Ri (Rit) is 1/4 for radiosonde,
772 and it increases from 1/4 to 2 for ERA5 reanalysis. Note that HVRRS data were
773 vertically resampled to 100_-m, 200_-m, 300_-m, and 400_-m at these four height
774 intervals to match with the ERA5 reanalysis. In addition, the moving average number
775 in Eq.(1) is 0. RS stands for radiosonde.

(a) Frequency of low Ri at 0.8–1.3 km a.g.l. (%) / Vertical resolution of RS is 100_-m

	Polar (NH)	Midlatitude (NH)	Subtropics (NH)	Tropics	Subtropics (SH)	Midlatitude (SH)	Polar (SH)
RS, $Rit=1/4$	14.76	22.76	22.13	13.28	20.95	22.44	20.46
ERA5, $Rit=1/4$	2.41	8.93	6.30	2.32	6.93	4.52	2.96
ERA5, $Rit=0.5$	3.73	12.80	9.43	3.60	11.95	8.42	7.34
ERA5, $Rit=1$	8.54	21.10	22.11	8.33	26.23	19.45	15.98
ERA5, $Rit=1.5$	13.80	29.69	31.44	12.98	36.88	28.83	24.03
ERA5, $Rit=2$	19.04	36.78	38.50	17.08	44.21	38.03	30.18

(b) Frequency of low Ri at 2.2–3.2 km a.g.l. (%) / Vertical resolution of RS is 200_-m

RS, $Rit=1/4$	3.00	5.60	7.40	5.48	8.87	4.29	4.12
ERA5, $Rit=1/4$	0.22	0.60	1.00	1.33	2.29	0.28	0.11

ERA5, $R_{it}=0.5$	0.37	1.03	1.96	2.10	4.23	0.50	0.18
ERA5, $R_{it}=1$	1.10	3.26	6.35	5.23	10.00	2.20	0.93
ERA5, $R_{it}=1.5$	2.64	6.75	12.30	9.02	16.39	5.62	2.68
ERA5, $R_{it}=2$	4.80	10.85	18.25	13.01	22.90	9.87	5.10

(c) Frequency of low Ri at 6–15 km a.g.l. (%) / Vertical resolution of RS is 300_-m

RS, $R_{it}=1/4$	0.75	2.20	3.86	6.00	4.44	1.98	0.56
ERA5, $R_{it}=1/4$	0.17	0.38	0.54	1.47	0.57	0.25	0.05
ERA5, $R_{it}=0.5$	0.32	1.16	1.95	4.37	2.10	0.93	0.15
ERA5, $R_{it}=1$	1.38	4.33	7.73	13.14	8.90	3.52	0.61
ERA5, $R_{it}=1.5$	2.93	8.32	14.54	21.79	17.05	6.76	1.38
ERA5, $R_{it}=2$	4.70	12.35	20.91	29.28	24.55	10.02	2.32

(d) Frequency of low Ri at 20–21 km a.g.l. (%) / Vertical resolution of RS is 400_-m

RS, $R_{it}=1/4$	0.03	0.07	0.12	0.04	0.04	0.10	0.07
ERA5, $R_{it}=1/4$	0.01	0.02	0.01	0.02	0.02	0.03	0.04
ERA5, $R_{it}=0.5$	0.02	0.03	0.01	0.02	0.03	0.04	0.04
ERA5, $R_{it}=1$	0.03	0.05	0.04	0.05	0.05	0.08	0.04
ERA5, $R_{it}=1.5$	0.04	0.11	0.13	0.19	0.09	0.17	0.04
ERA5, $R_{it}=2$	0.05	0.21	0.32	0.55	0.18	0.30	0.05

776

777

778

779

780

781

782

783

784

785

786

787
788
789
790
791
792
793
794
795
796
797

798 **Table 3.** Vertical wind shears at 0.8–1.3 km a.g.l. (a), 2.2–3.2 km a.g.l. (b), 6–15 km
799 a.g.l. (c), and 20–21 km a.g.l. (d). Note that HVRRS data was vertically resampled to
800 100_-m, 200_-m, 300_-m, and 400_-m at these four height intervals to match with the
801 ERA5 reanalysis. RS stands for radiosonde.

(a) Wind shear at 0.8–1.3 km a.g.l. (m/s/km) / Vertical resolution of RS is 100_-m							
	Polar	Midlatitude	Subtropics	Tropics	Subtropics	Midlatitude	Polar
	(NH)	(NH)	(NH)		(SH)	(SH)	(SH)
RS	12.50	11.89	11.29	11.51	13.32	13.06	14.04
ERA5	5.50	6.14	6.67	4.92	7.09	7.00	6.23
(b) Wind shear at 2.2–3.2 km a.g.l. (m/s/km) / Vertical resolution of RS is 200_-m							
RS	8.26	9.00	9.11	8.67	9.22	9.39	9.75
ERA5	3.70	4.50	5.25	4.67	5.44	4.73	4.20
(c) Wind shear at 6–15 km a.g.l. (m/s/km) / Vertical resolution of RS is 300_-m							
RS	8.30	9.58	9.54	7.76	9.88	9.38	8.06
ERA5	4.01	5.39	6.02	5.26	6.32	4.86	3.39
(d) Wind shear at 20–21 km a.g.l. (m/s/km) / Vertical resolution of RS is 400_-m							
RS	9.07	10.37	11.55	12.50	11.99	10.48	9.94

ERA5	2.99	3.85	4.80	5.63	4.73	3.64	2.98
------	------	------	------	------	------	------	------

802
803
804
805
806
807
808
809
810
811
812

813 **Table 4.** Similar to Tab.1 but for the occurrence frequency of $Ri < Rit$. Note that Rit is
814 indicated by $Ri < 1/4$ in radiosonde, but it is identified with 1 in ERA5 reanalysis.

(a) $OF(Ri < Rit)$ at 0–2 km a.g.l. (%)

	Polar (NH)	Midlatitude (NH)	Subtropics (NH)	Tropics	Subtropics (SH)	Midlatitude (SH)	Polar (SH)
HVRRS	9.05	15.57	16.44	13.13	17.30	15.21	13.40
ERA5	28.02	41.26	40.36	40.14	47.45	42.92	27.59

(b) $OF(Ri < Rit)$ at 10–15 km a.g.l. (%)

HVRRS	0.51	2.05	5.21	11.11	6.00	1.53	0.65
ERA5	0.44	2.62	6.86	17.03	7.15	1.67	0.28

(c) $OF(Ri < Rit)$ at 20–25 km a.g.l. (%)

HVRRS	0.45	0.48	0.42	0.51	0.38	0.67	1.53
ERA5	0.06	0.07	0.04	0.11	0.06	0.06	0.04

815
816
817
818

819

820

821

822

823

824

825

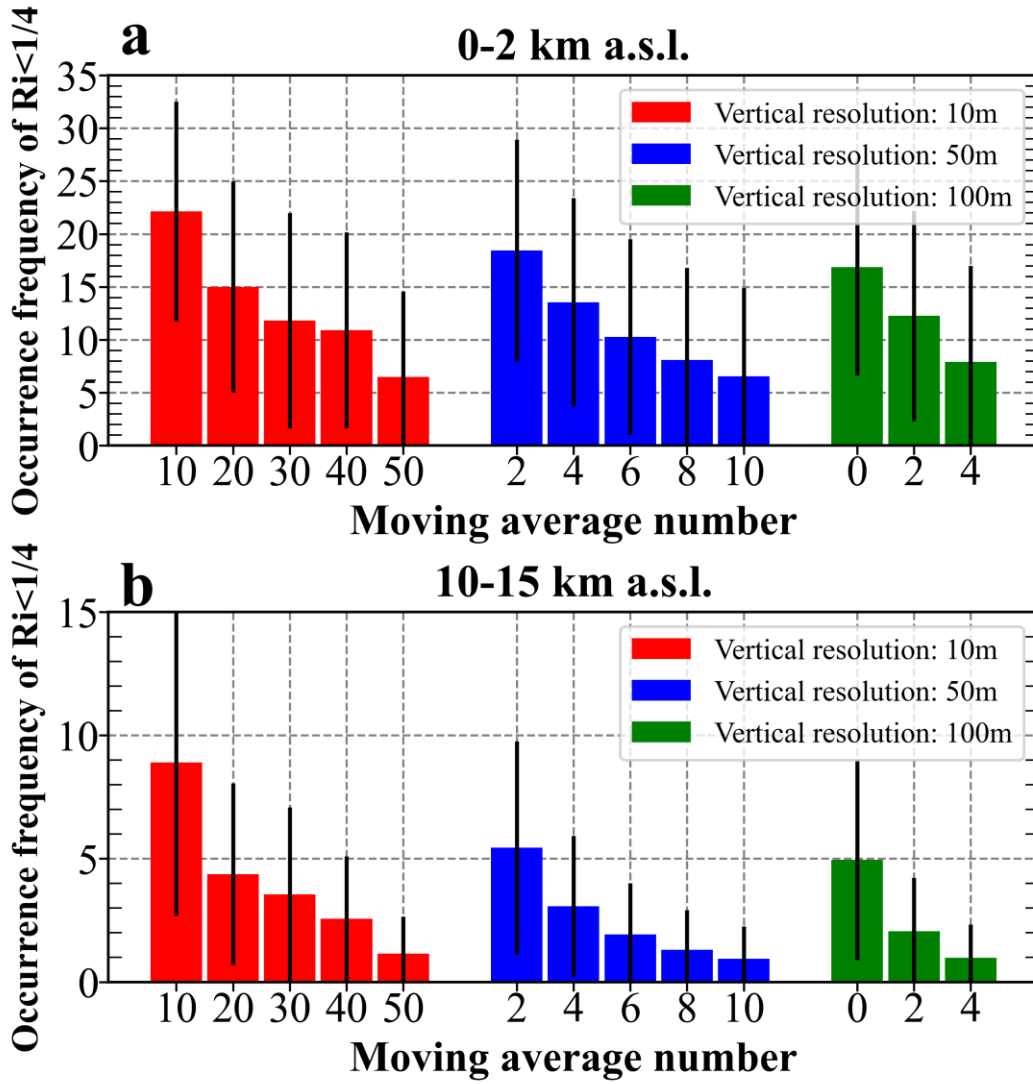
826

827

828

829

830



831

832 **Figure 1.** The averaged occurrence frequencies of $Ri < 1/4$ at heights of 0–2 km a.s.l. (a)

833 and 10–15 km a.s.l. (b), with vertical resolutions ranging 10_-m to 100_-m and moving

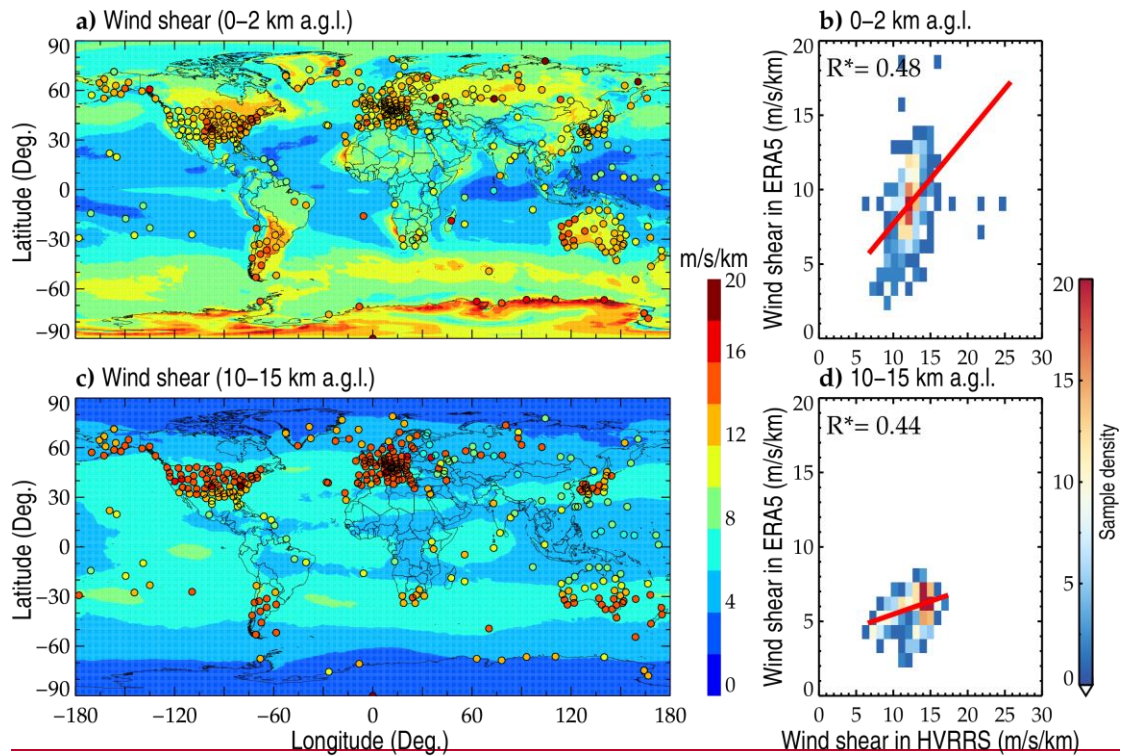
834 point numbers increasing from 0 to 50. The error bars correspond to the standard

835 deviation. The metrics are counted based on all radiosonde profiles during years 2017–

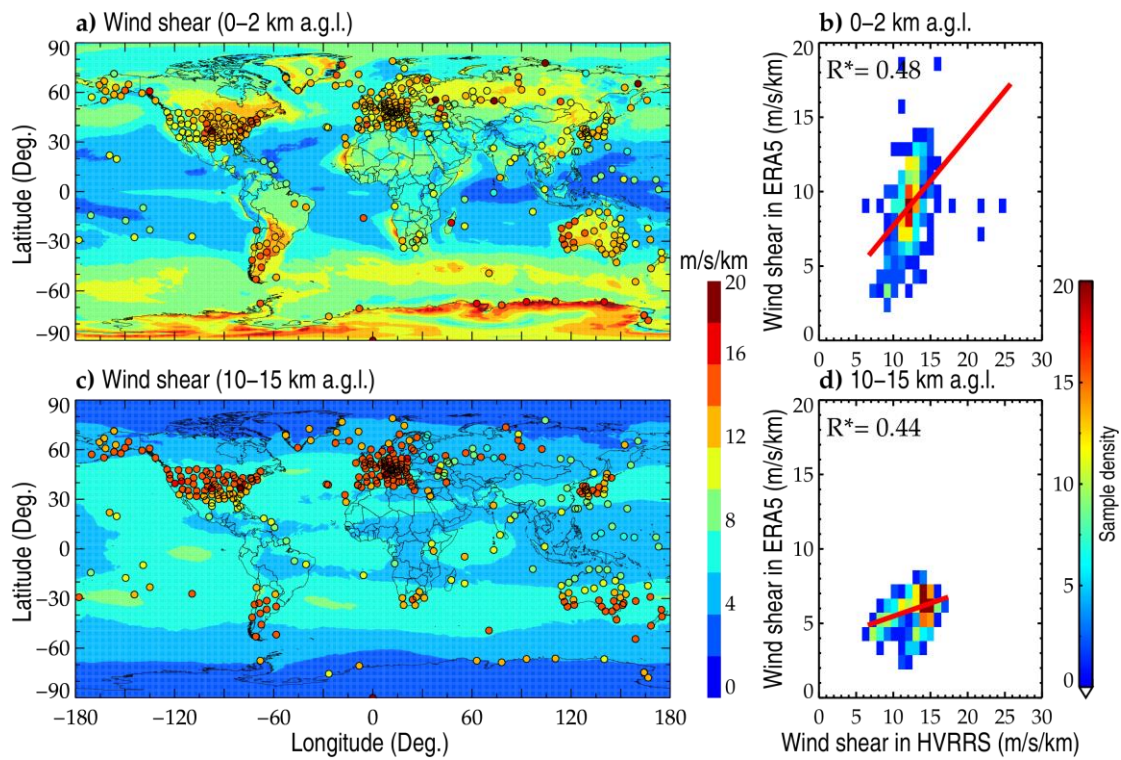
836 2022.

837

838



839

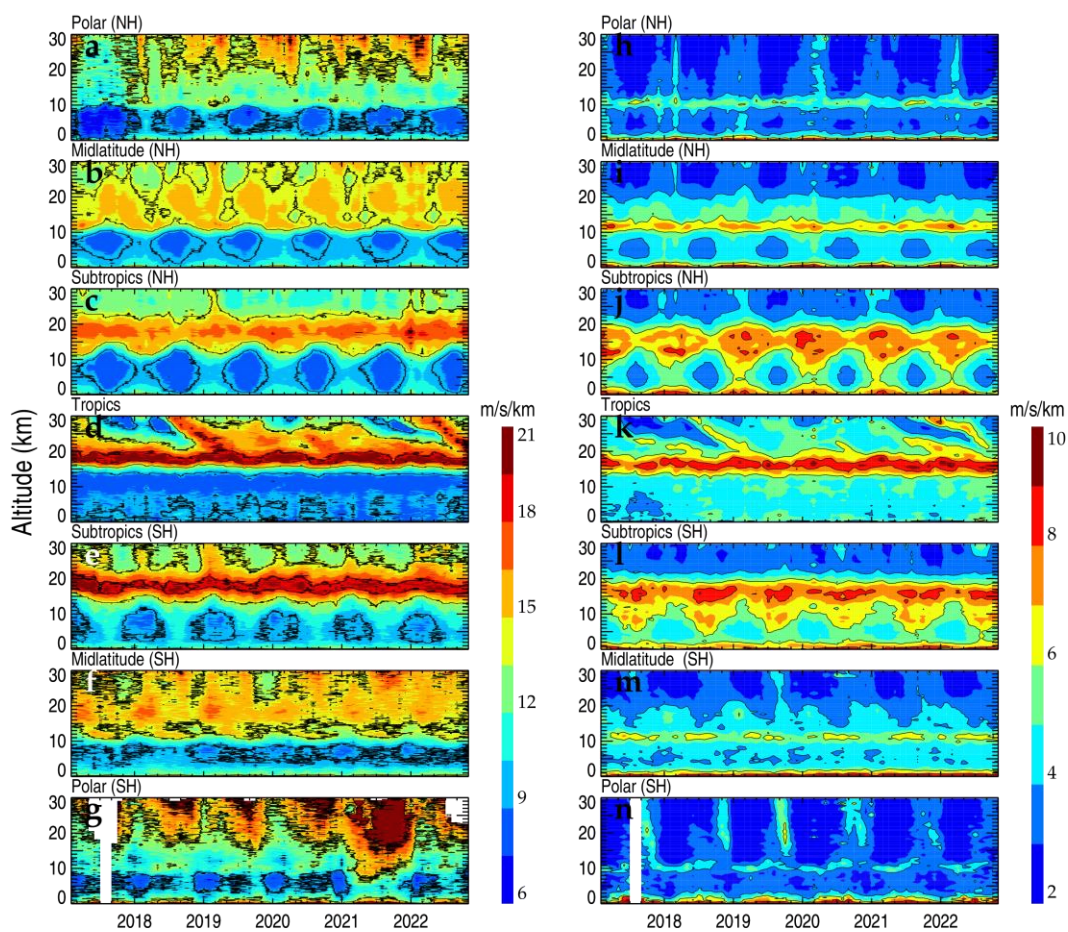


840

841 **Figure 2.** The spatial distribution of mean wind shear in ERA5 reanalysis at heights of
 842 0–2 km a.g.l. (a) and 10–15 km a.g.l. (c). The overlaid colored circles represent the
 843 result in HVRRS at the same height levels. Each data point represents a vertically
 844 averaged value of the wind shear at one radiosonde station during the whole study
 845 period. Density plots (b, d) show the correlation between wind shears in HVRRS and

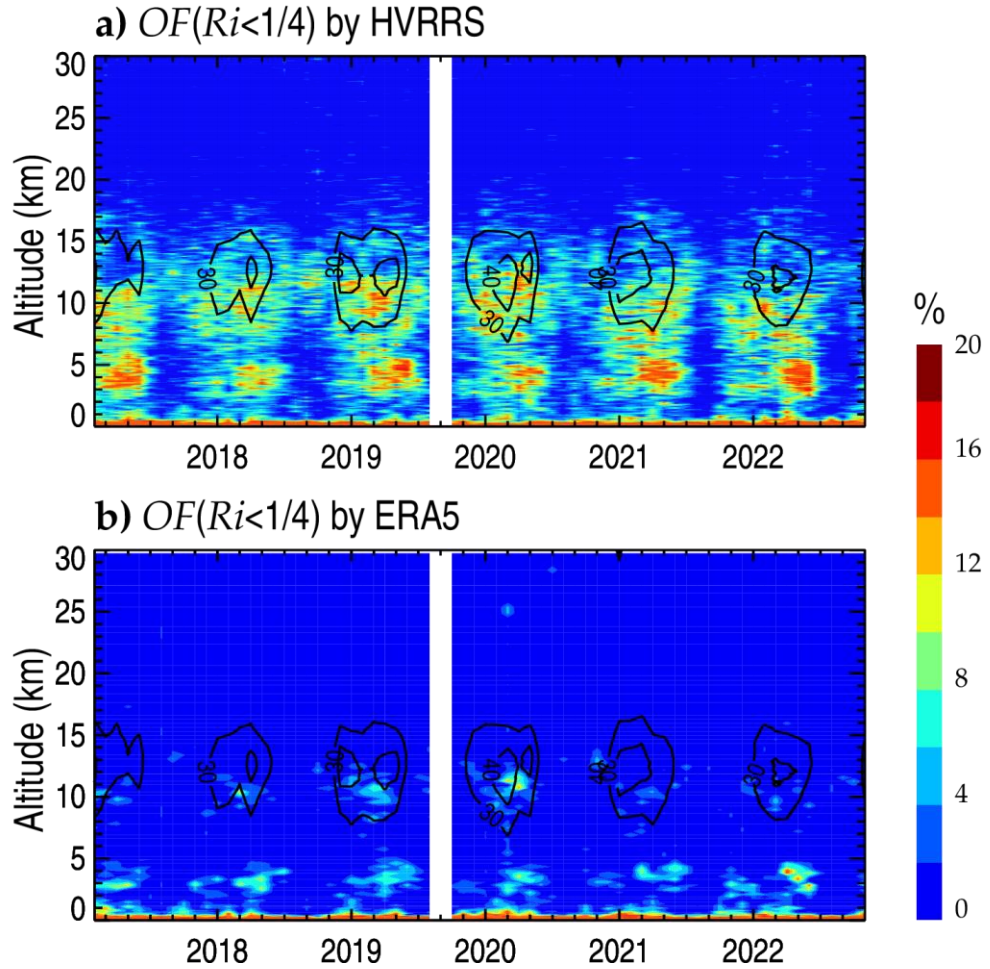
846 ERA5 reanalysis. The ERA5 derived wind shears are spatially and temporally
 847 collocated with those of HVRRS. In addition, the red lines represent a least-squared
 848 linear regression, and the star superscripts indicate that values are statistically
 849 significant ($p < 0.05$).

850
 851
 852



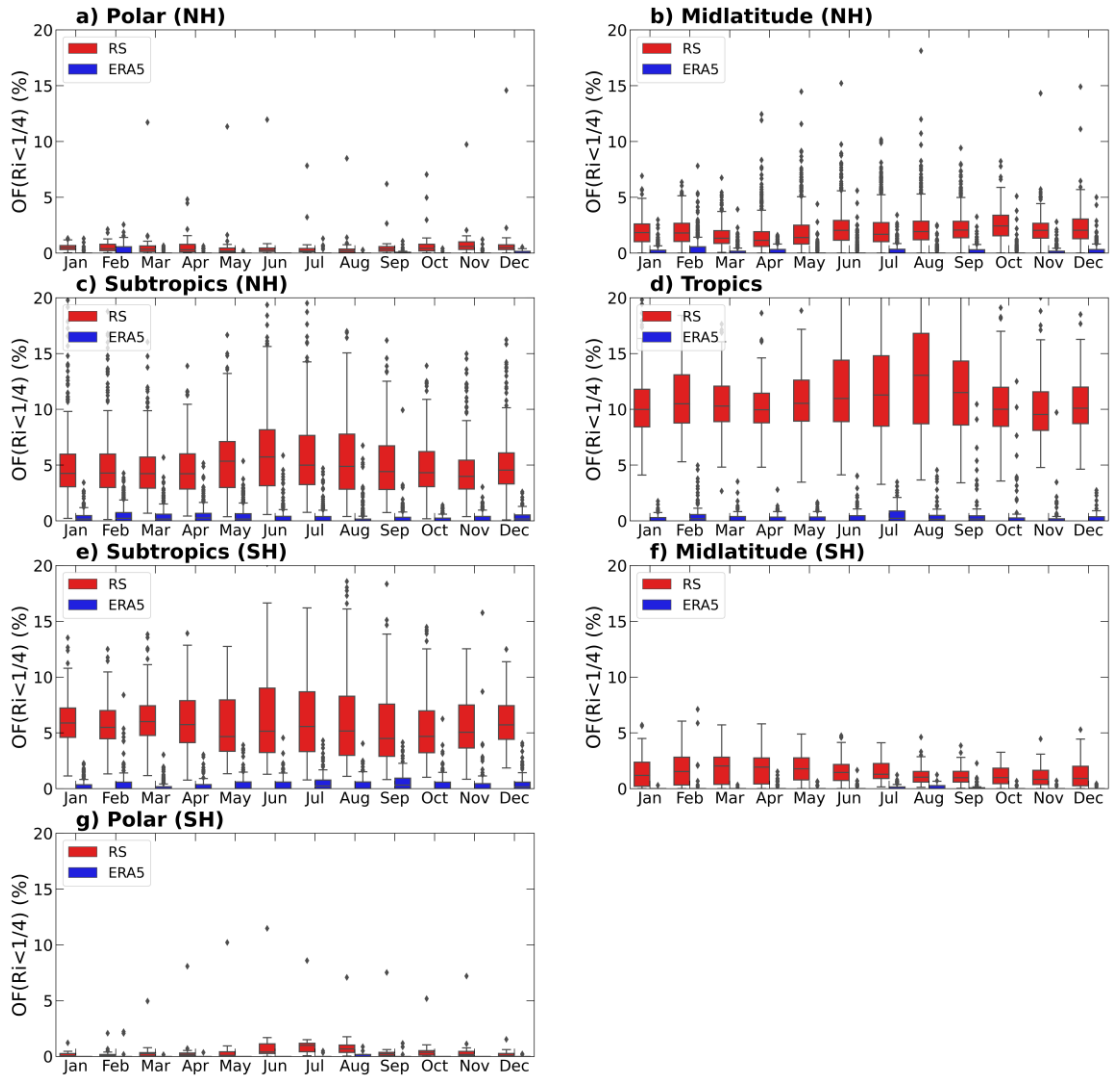
853

854 **Figure 3.** Monthly mean wind shears during years 2017–2022 in HVRRS (a–g) and
 855 ERA5 reanalysis (h–n) at different climate zones. The ERA5 derived wind shears are
 856 spatially and temporally collocated with those of HVRRS. NH=Northern Hemisphere;
 857 SH=Southern Hemisphere.



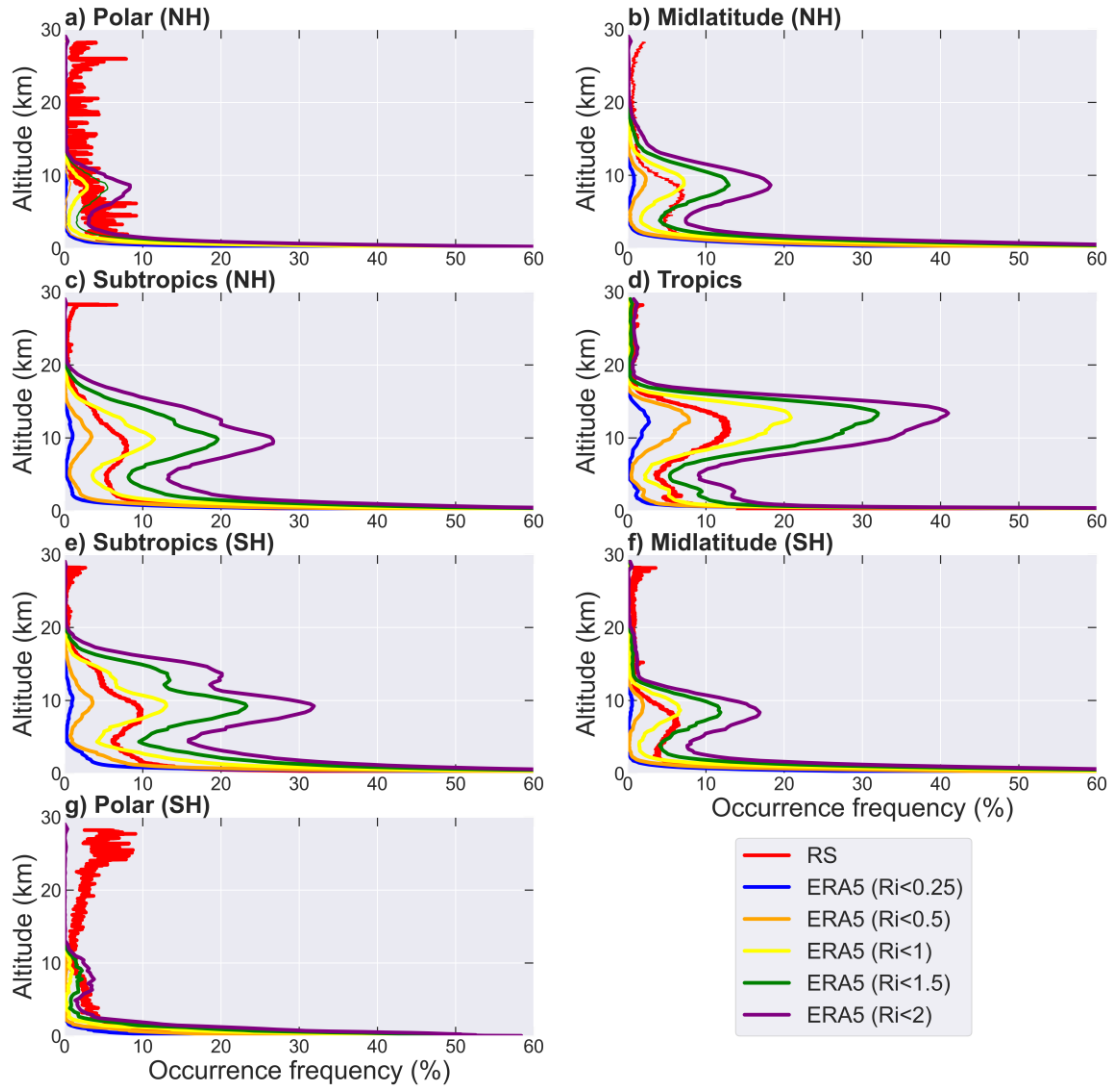
858

859 **Figure 4.** The monthly occurrence frequency of $Ri < 1/4$ at Corpus Christi station (27.77°
 860 N, -97.5° W) in HVRRS (a) and ERA5 reanalysis (b). Note that the contour curves in
 861 (a) and (b) concern the mean horizontal wind speed, and that the ERA5 derived
 862 quantities are spatially and temporally collocated with those of HVRRS.



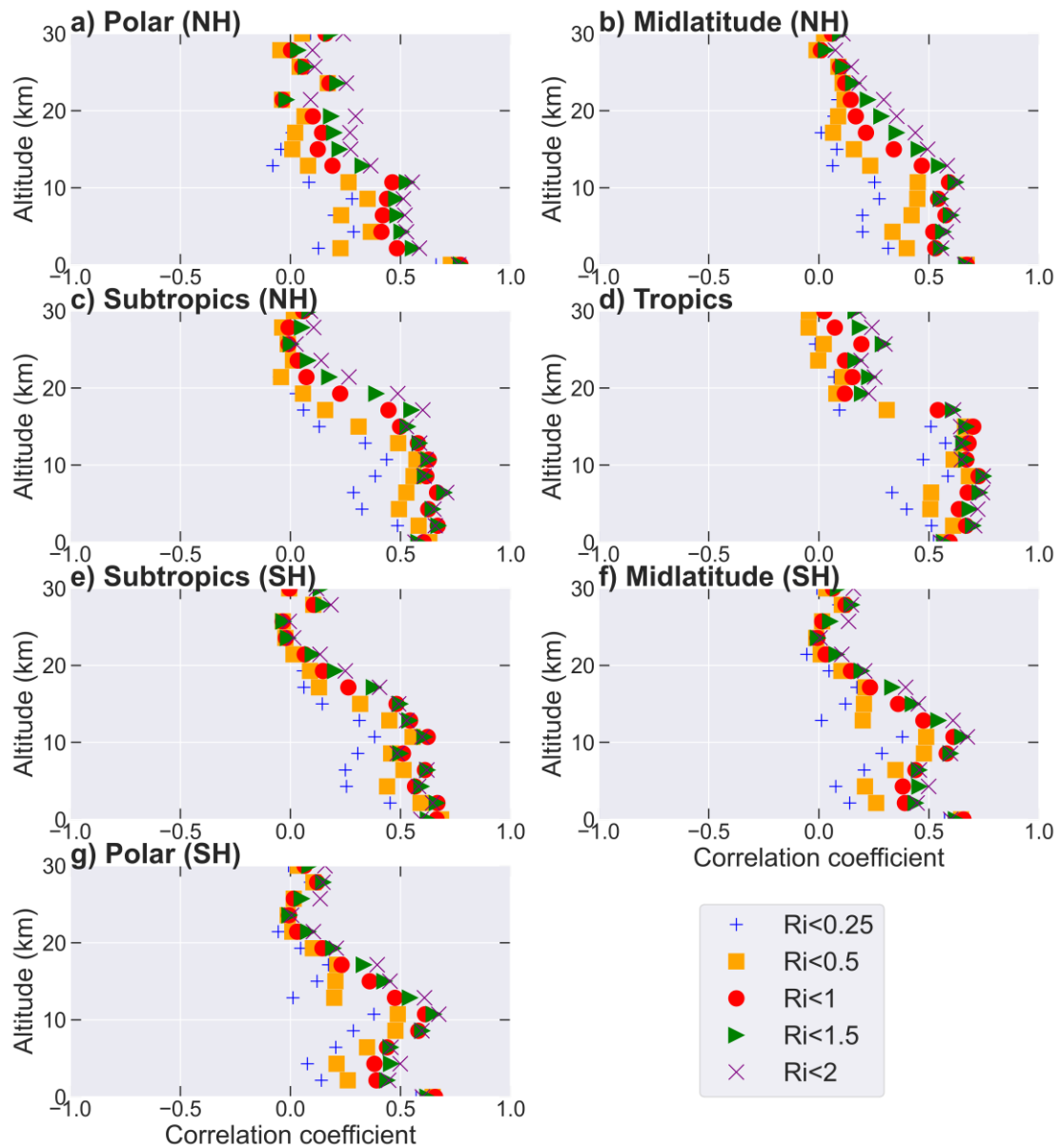
863

864 **Figure 5.** The annual cycles of the occurrence frequency of $Ri < 1/4$ in different climate
 865 zones at 10–15 km a.g.l. The red and blue boxes represent the frequencies in HVRRS
 866 and ERA5 reanalysis, respectively. The ERA5 derived Ri is spatially and temporally
 867 collocated with that of HVRRS. NH, Northern Hemisphere; SH, Southern Hemisphere.



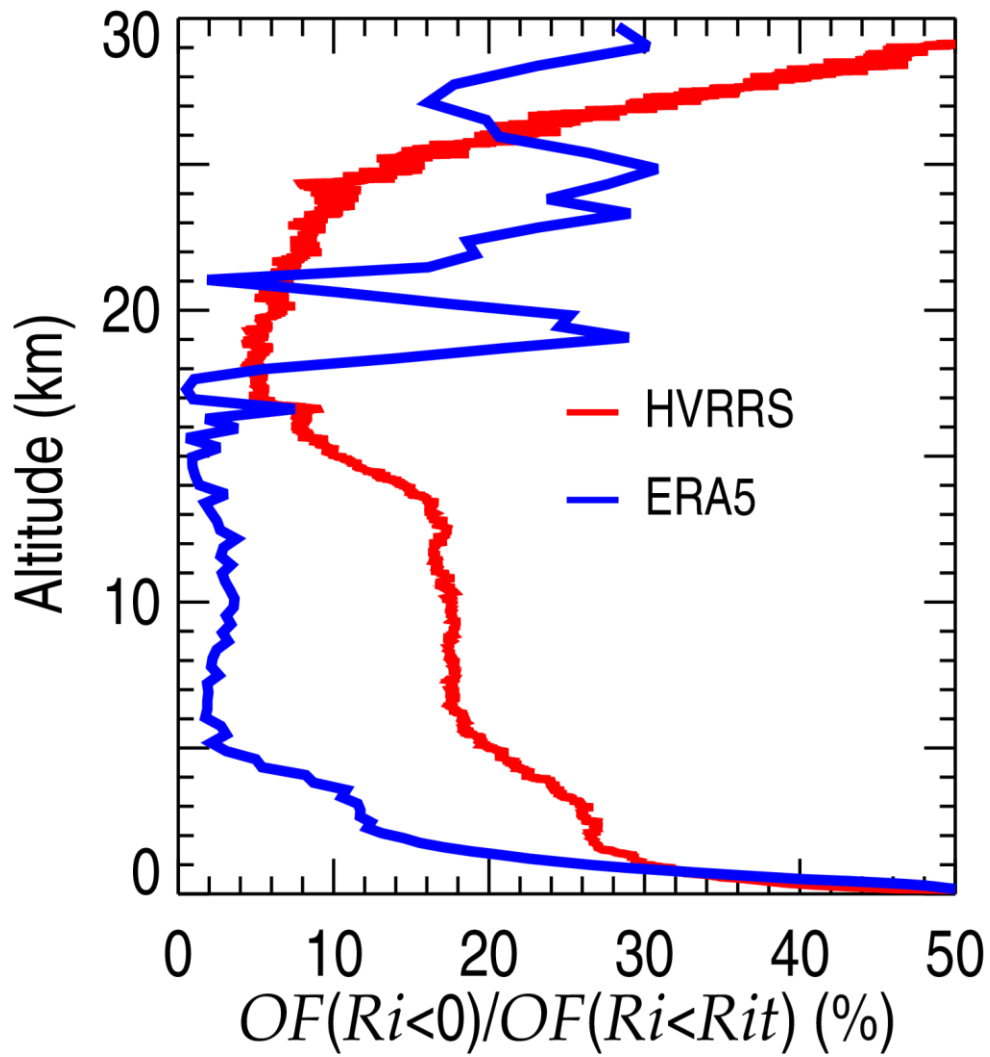
868

869 **Figure 6.** The altitude variation of the occurrence frequency of Ri below certain
 870 thresholds (0.25, 0.5, 1, 1.5, and 2) in ERA5 reanalysis in various climate zones. The
 871 ERA5 derived Ri is spatially and temporally collocated with that of HVRRS. The
 872 occurrences of $Ri < 1/4$ in HVRRS are overlapped with red lines.



873

874 **Figure 7.** The correlation coefficients between monthly averaged occurrence frequency
 875 of $Ri < 1/4$ in the HVRRS and the monthly occurrence frequency of Ri below certain
 876 thresholds (0.25, 0.5, 1, 1.5, and 2) in ERA5 reanalysis. The ERA5 derived Ri is
 877 spatially and temporally collocated with that of HVRRS. The coefficients in various
 878 climate zones are estimated in an increment of 2 km.



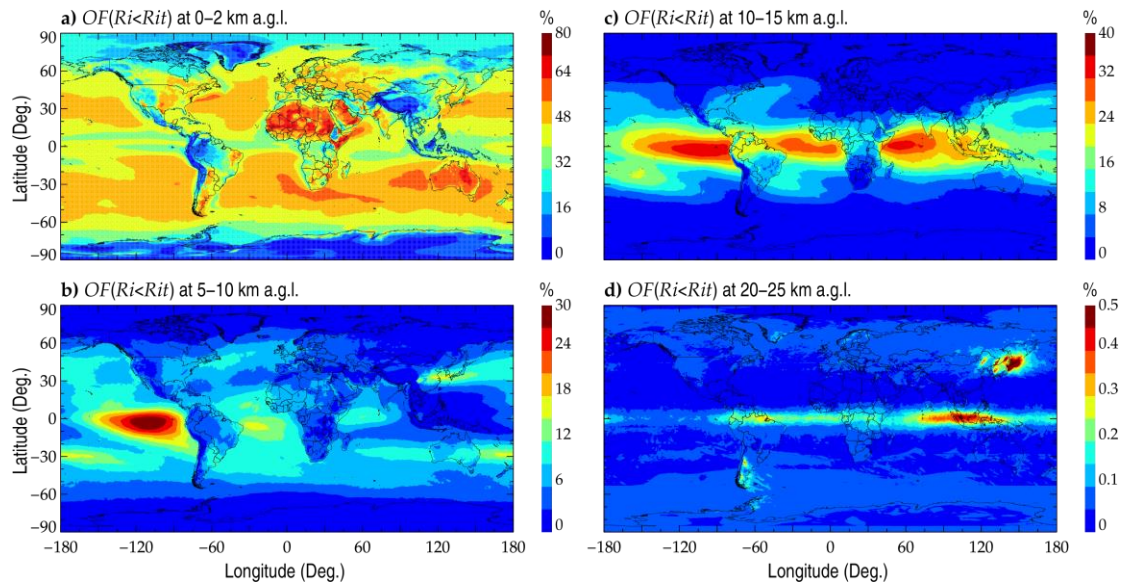
879

880 **Figure 8.** The percentage of $OF(Ri < 0)$ relative to $OF(Ri < Rit)$ in HVRRS (red) and
 881 ERA5 reanalysis (blue).

882

883

884



885

886

887

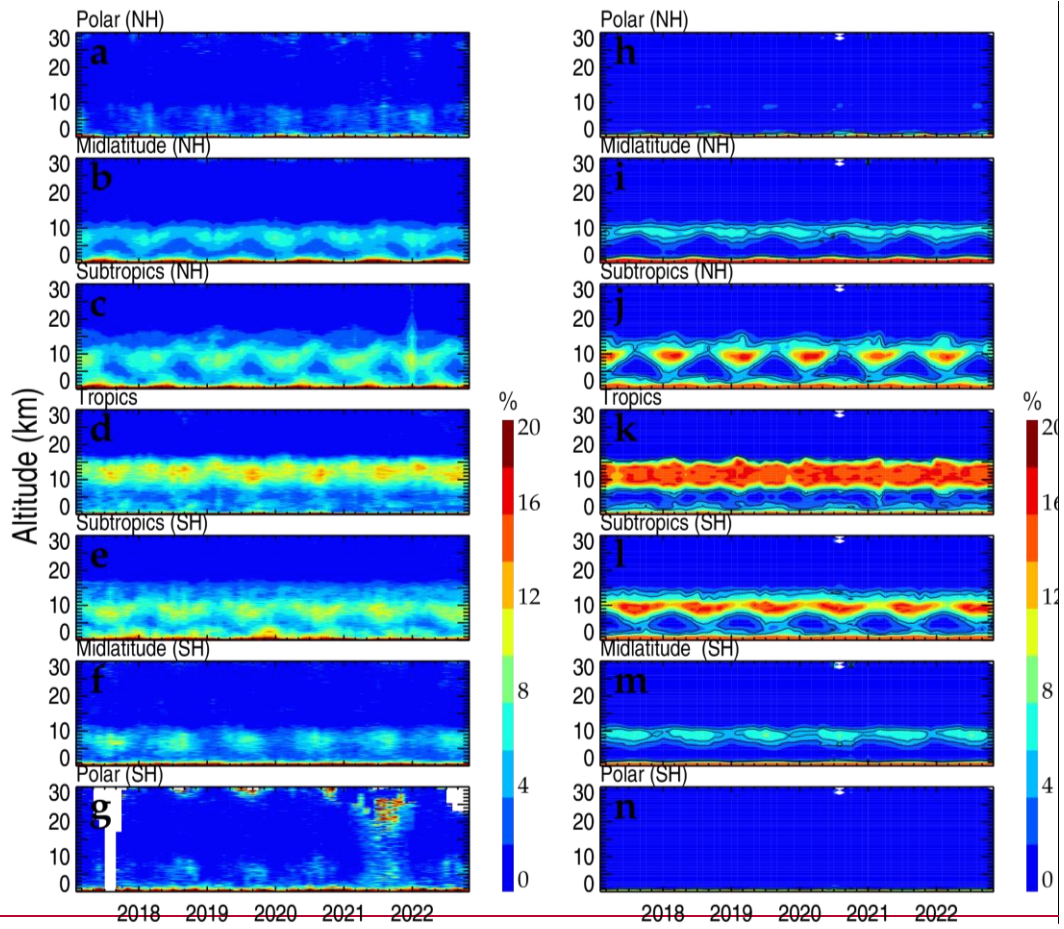
888

889

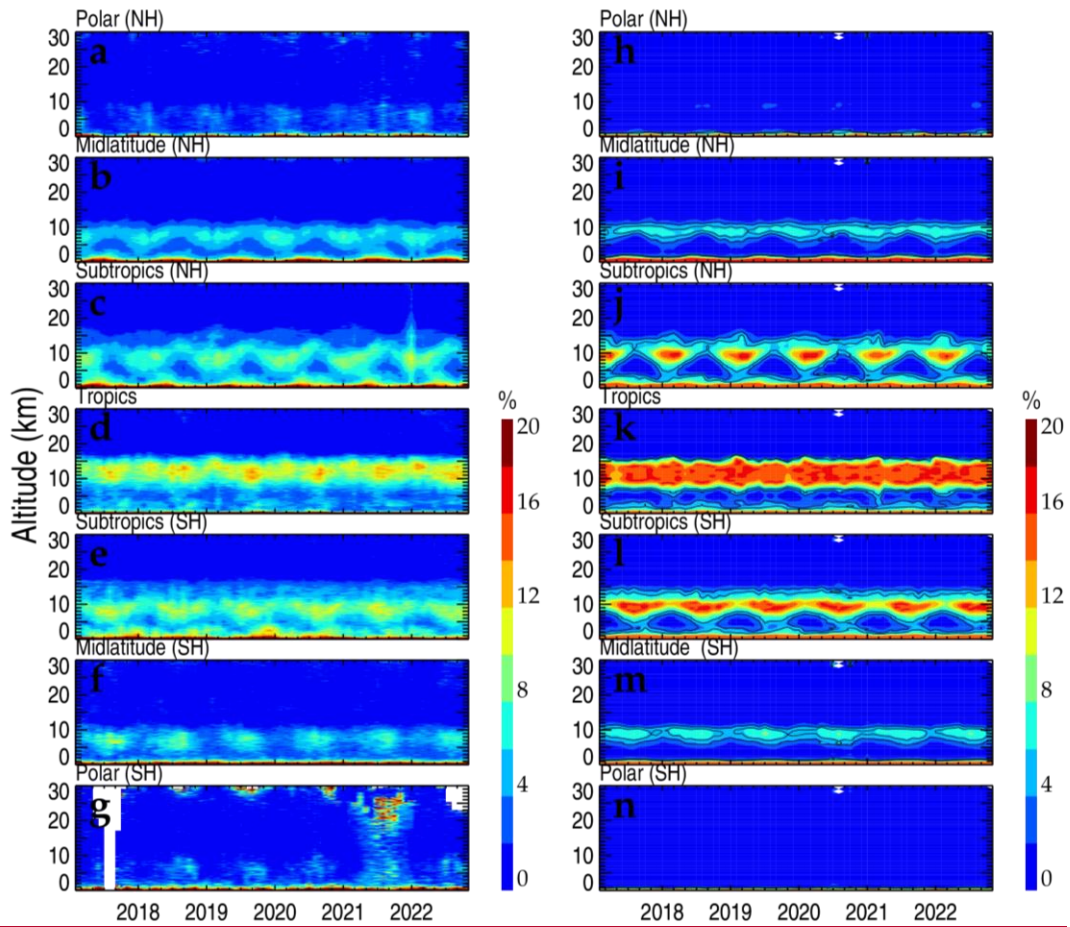
890

891

Figure 9. The spatial distribution of the mean $OF(Ri < Rit)$ in ERA5 reanalysis at 0–2 km a.g.l. (a), 5–10 km a.g.l. (b), 10–15 km a.g.l. (c), and 20–25 km a.g.l. (d). Note that Rit is set to 1.

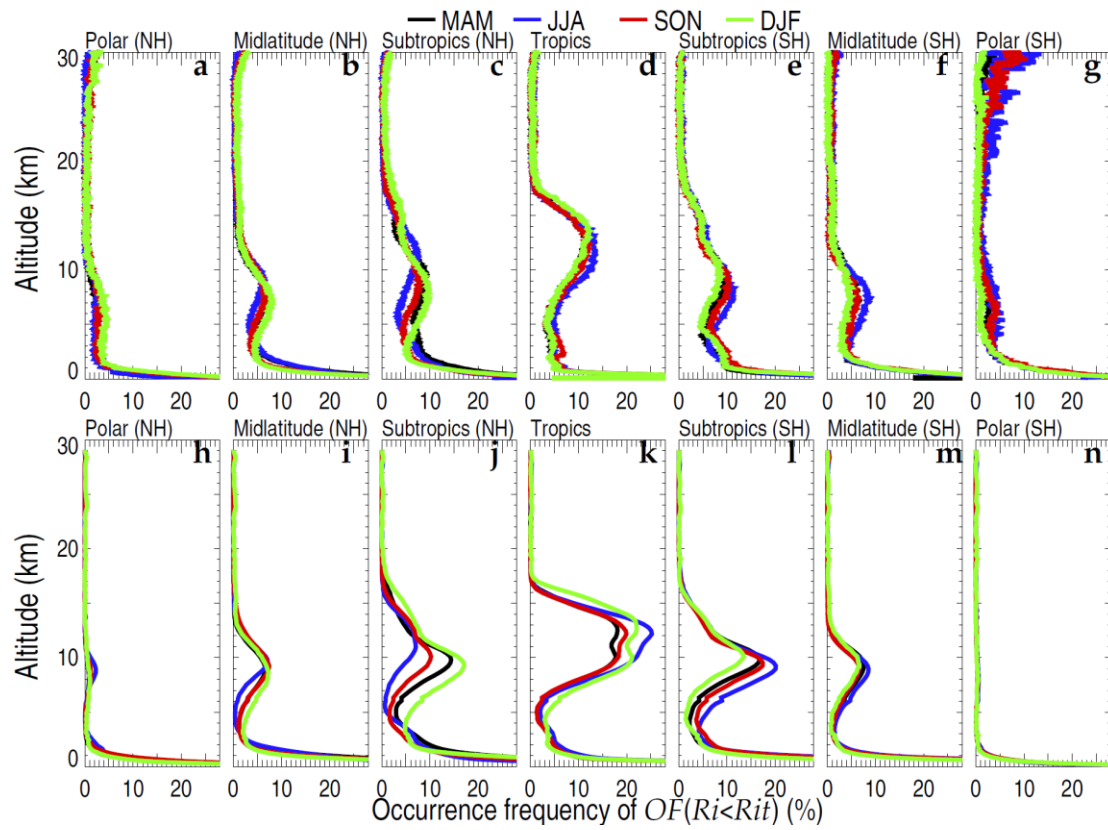


892



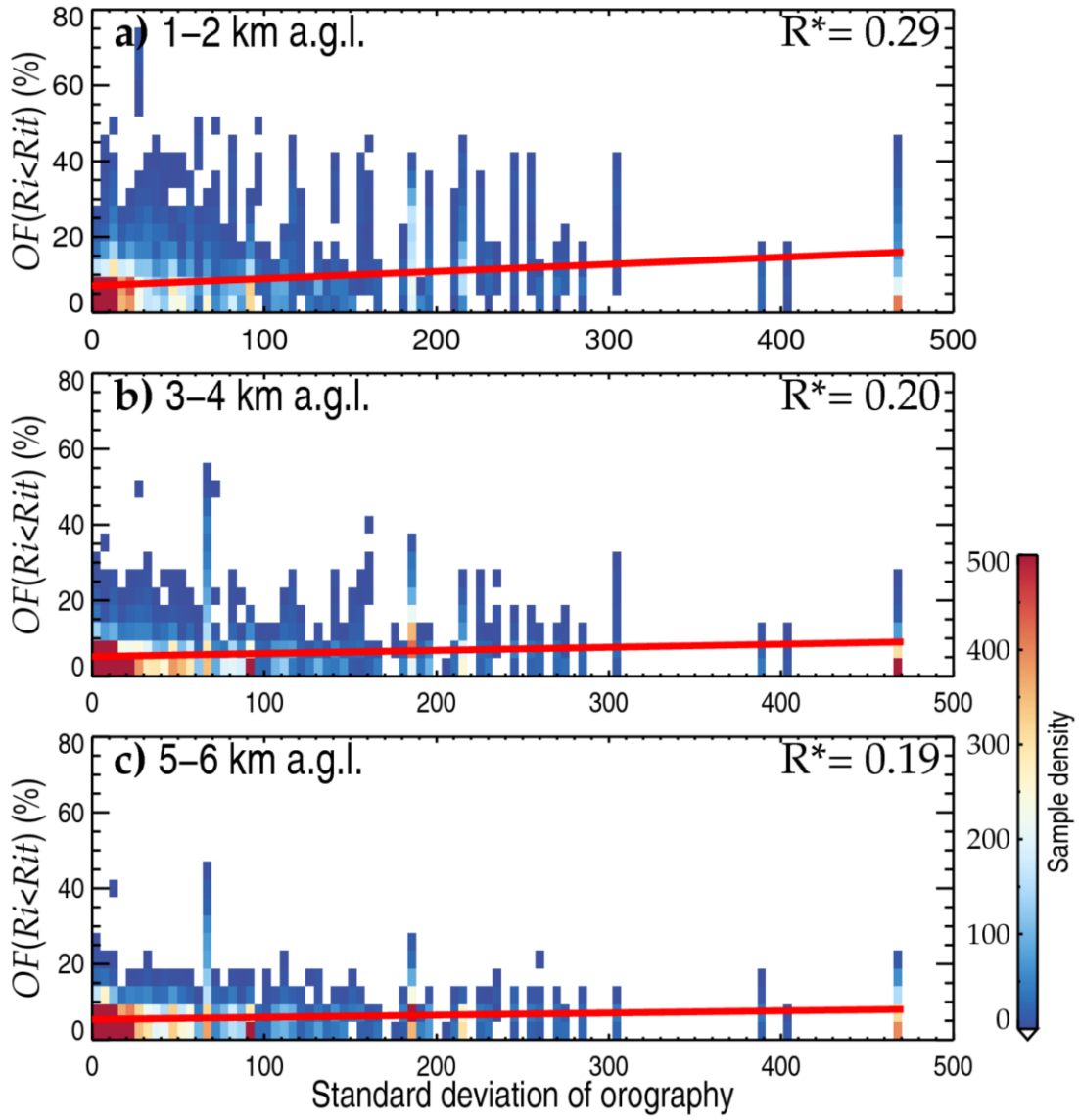
893

894 **Figure 10.** The monthly averaged $OF(Ri < Rit)$ in the HVRRS (a–g) and ERA5
 895 reanalysis (h–n) in seven climate zones. NH=Northern Hemisphere; SH=Southern
 896 Hemisphere.

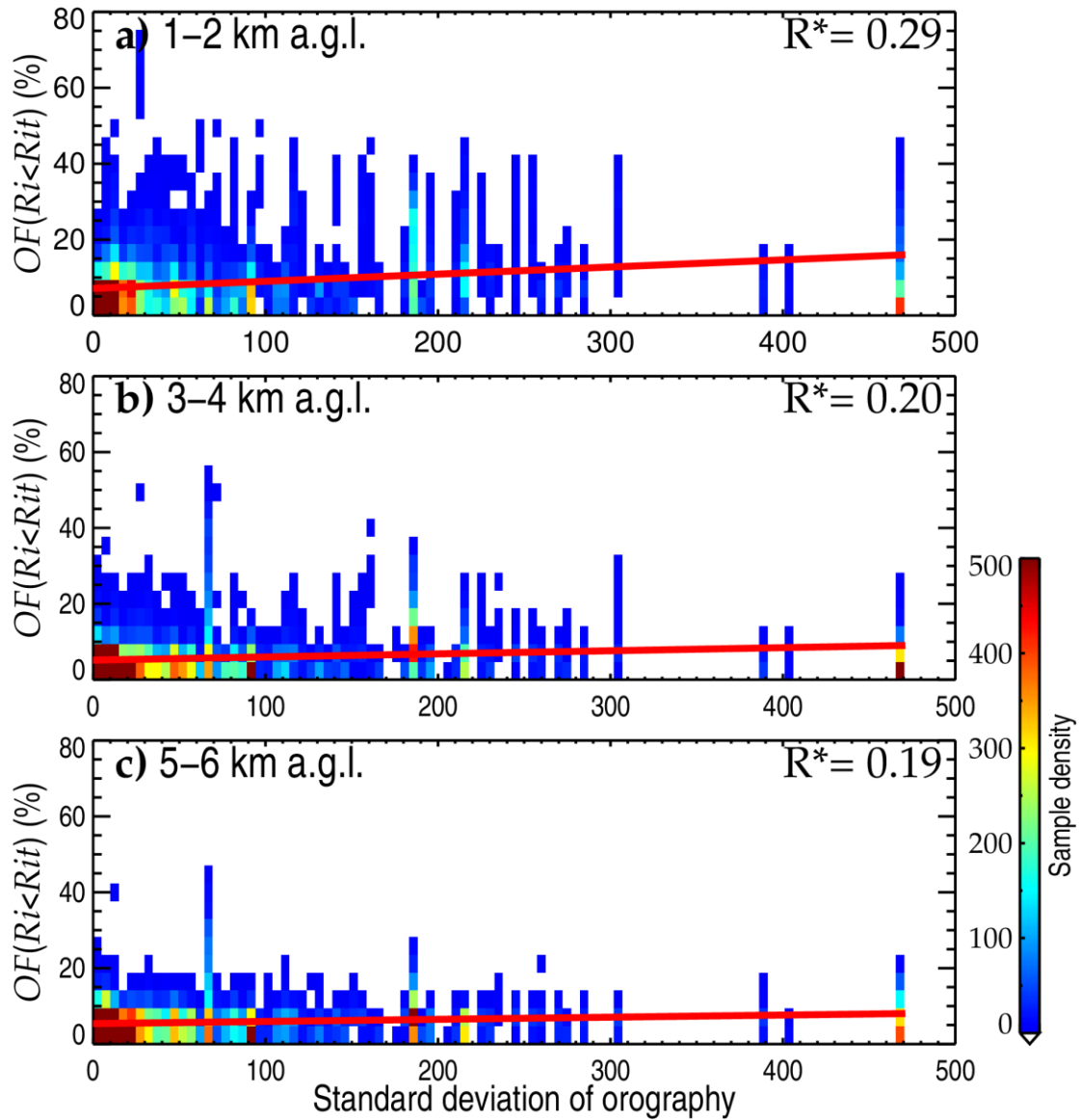


897

898 **Figure 11.** The seasonal averaged $OF(Ri < Rit)$ in the HVRRS (a–g) and ERA5
 899 reanalysis (h–m) in seven climate zones. MAM, March–April–May; JJA, June–July–
 900 August; SON, September–October–November; DJF, December–January–February.
 901 NH=Northern Hemisphere; SH=Southern Hemisphere.



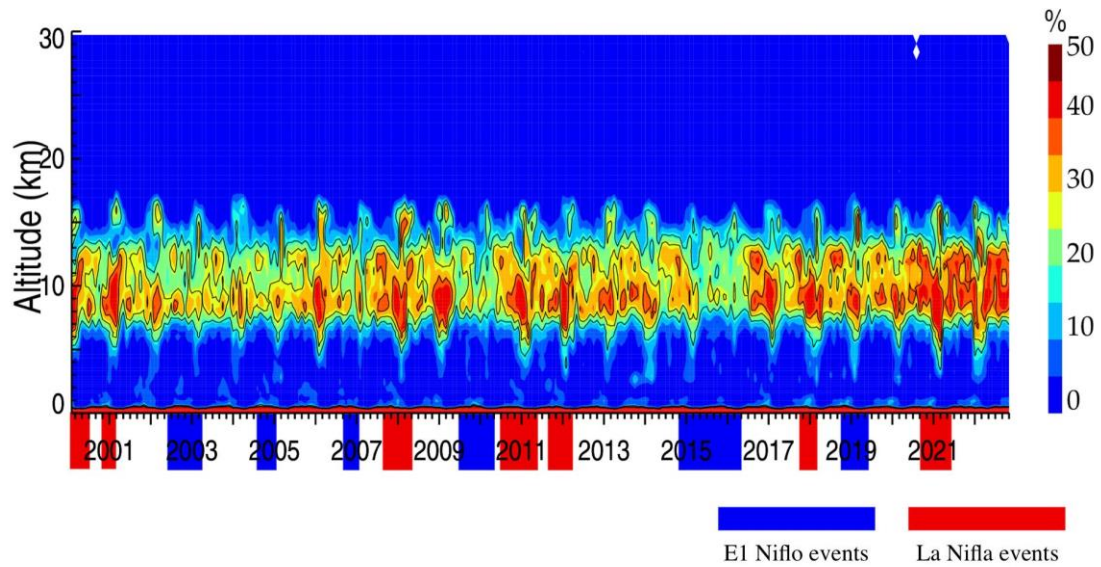
902



903

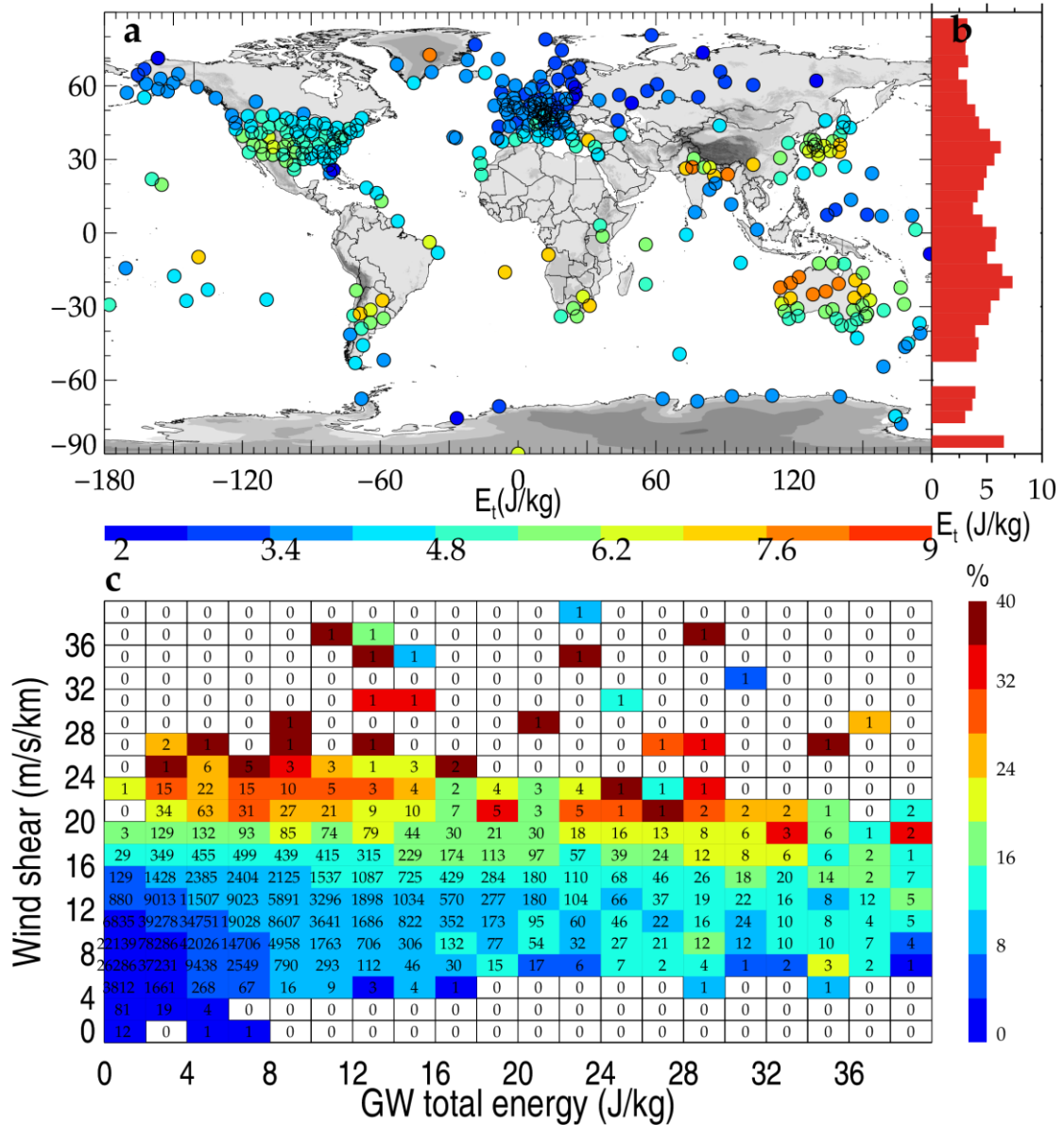
904 **Figure 12.** The association of HVRRS-determined $OF(Ri < Rit)$ with different standard
 905 deviations of orography (dimensionless). (a), (b), and (c) are for height ranges of 1–2
 906 km, 3–4 km, and 5–6 km a.g.l., respectively. The correlation coefficients between
 907 $OF(Ri < Rit)$ and standard deviation of orography are marked in the top right corner,
 908 where the star superscripts indicate that values are statistically significant ($p < 0.05$).

909



910

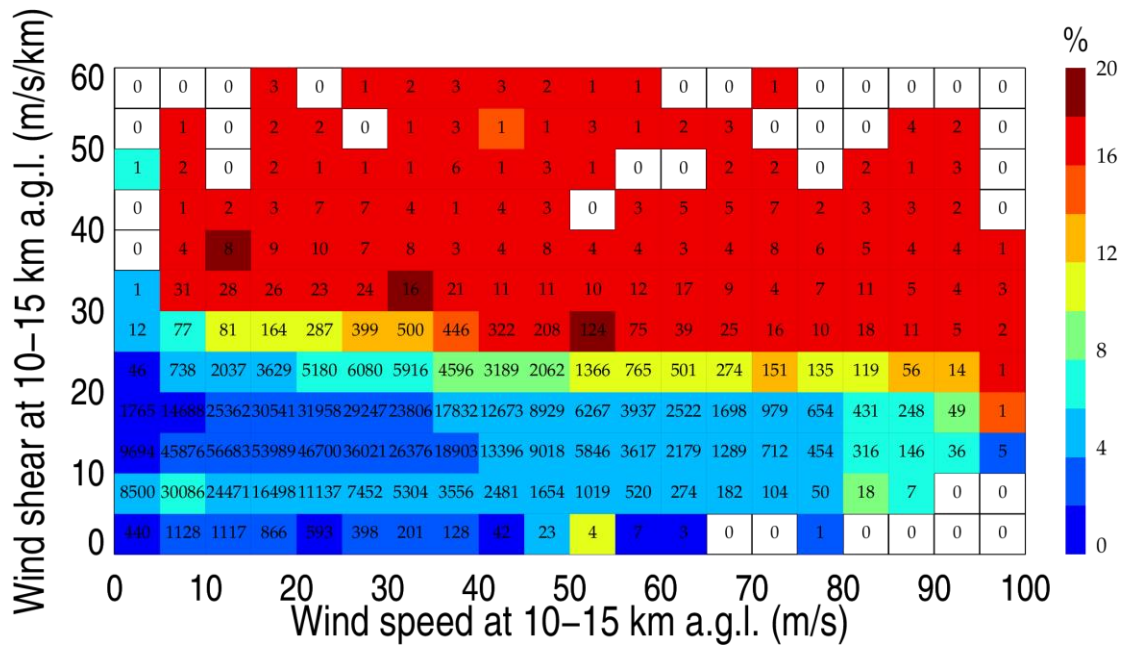
911 **Figure 13.** The monthly averaged $OF(Ri < Rit)$ in ERA5 reanalysis over the Niño 3
912 region (5°N – 5°S , 150°W – 90°W). The blue and red shadings in time axis indicate the
913 time periods with El Niño and La Niña events, respectively.



914

915 **Figure 14.** Geographical distribution of mean tropospheric GW total energy obtained
 916 from the HVRRS (a). The latitudinal variation of mean energy in a grid cell of 5°
 917 latitude (b). The joint distribution of $OF(Ri < Rit)$ with GW energy and wind shear (c).
 918 The $OF(Ri < Rit)$ and wind shear are derived from individual HVRRS profiles and
 919 vertically averaged over the tropospheric segment that is used for GW study. The
 920 numerical number in (c) indicates the matched profile number in each grid, using a bin
 921 size of 2 J/kg along the x axis and 2 m/s/km along the y axis.

922



923

924 **Figure 15.** Joint distribution of HVRRS-derived wind speed, wind shear, and
 925 $OF(Ri < Rit)$, with a bin size of 5 m/s along the x axis and 5 m/s/km along the y axis.
 926 Note that all the relationship is based on the mean result of individual profiles at heights
 927 of 10–15 km a.g.l.. The number indicates the matched profile number in each grid.